On the choice of finite element for applications in geodynamics

Cedric Thieulot[1] and Wolfgang Bangerth[2]

[1]Department of Earth Sciences, Utrecht University, Utrecht, The Netherlands
[2]Department of Mathematics, Department of Geosciences, Colorado State University, Fort Collins, CO, USA

Correspondence: C. Thieulot (c.thieulot@uu.nl)

Abstract. Geodynamical simulations over the past decades have widely been built on quadrilateral and hexahedral finite elements. For the discretisation of the key Stokes equation describing slow, viscous flow, most codes use either the unstable $Q_1 \times P_0$ element, a stabilised version of the equal-order $Q_1 \times Q_1$ element, or more recently the stable Taylor-Hood element with continuous ($Q_2 \times Q_1$) or discontinuous ($Q_2 \times P_{-1}$) pressure. However, it is not clear which of these choices is actually the best at accurately simulating "typical" geodynamic situations.

Herein, we are providing for the first time a systematic comparison of all of these elements. We use a series of benchmarks that illuminate different aspects of the features we consider typical of mantle convection and geodynamical simulations. We will show in particular that the stabilised $Q_1 \times Q_1$ element has great difficulty producing accurate solutions for buoyancy-driven flows – the dominant forcing for mantle convection flow – and that the $Q_1 \times P_0$ element is too unstable and inaccurate in practice. As a consequence, we believe that the $Q_2 \times Q_1$ and $Q_2 \times P_{-1}$ elements provide the most robust and reliable choice for geodynamical simulations, despite the greater complexity in their implementation and the substantially higher computational cost when solving linear systems.

Contents

Solid Earth
Discussions

Open Access

EGU

1   Introduction

For the past several decades, the geodynamics community's workhorse for numerical simulations of the incompressible Stokes equations has been the use of (continuous) piecewise bi/tri-linear velocity and piecewise constant (discontinuous) pressure

30   finite elements, often in combination with the penalty method for the solution of the resulting linear systems (e.g. Donea and Huerta, 2003). This velocity-pressure pair is often referred to as the $Q_1 \times P_0$ Stokes element, and sometimes as the $Q_1 \times Q_0$ element (Gresho and Sani, 2000). It is used, for example, in the ConMan (King et al., 1990), SOPALE (Fullsack, 1995), CitcomCU (Moresi and Gurnis, 1996; Zhong, 2006), CitcomS (Zhong et al., 2000; McNamara and Zhong, 2004; Zhong et al., 2008), Ellipsis (Moresi et al., 2003; O'Neill et al., 2006), UnderWorld (Moresi et al., 2003), DOUAR (Braun et al., 2008), and

35   FANTOM (Thieulot, 2011) codes and has therefore been used in hundreds of publications.

The popularity of this element can be explained by its very small memory footprint and ease of implementation and use. On the other hand, it has a rather low convergence order that makes it difficult to achieve high accuracy; maybe more importantly, the element is known not to satisfy the so-called LBB condition (e.g. Donea and Huerta, 2003) and is therefore unstable. This instability noticeably manifests itself through oscillatory pressure modes (e.g. Fig. 18 of Thieulot et al. (2008) or Fig. 36 of

40   Thieulot (2014)) and makes it not suited for large scale three-dimensional simulations coupled to iterative solvers (May and Moresi, 2008). The unreliability of the pressure also makes this element a dubious choice for models in which some of the parameters – e. g., the density or the viscosity – depend on the pressure.

The more modern alternative to this choice is the Taylor-Hood element that uses (continuous) polynomials of degree k for the velocity and of degree $k - 1$ for the pressure, where $k \geq 2$. This element is not only LBB-stable, but owing to its higher

45   polynomial degree is also convergent of higher order. It is therefore widely used in commercial flow solvers, and is also the default element for the ASPECT code in geodynamics (Kronbichler et al., 2012; Heister et al., 2017). This element is obviously more difficult to implement, and building efficient solvers and preconditioners is also more complicated (Kronbichler et al., 2012; Clevenger et al., 2020). However, this drawback can be mitigated by building on one of the widely available finite element libraries that have appeared over the past 20 years; for example, ASPECT inherits all of its finite element functionality from the

50   deal.II library (see Bangerth et al. (2007); Arndt et al. (2020)). We will note that one can also use variations of the underlying idea of the Taylor-Hood element, for example on quadrilaterals and hexahedra by using $Q_k \times P_{-(k-1)}$ (see for instance May et al. (2015)) in which the pressure is discontinuous and of (total) polynomial degree $k-1$, but missing the shape functions that distinguish the space Q_k on quadrilaterals/hexahedra from the space P_k that is typically used on triangles/tetrahedra. Another variation is to enrich the pressure space by a constant shape function on each cell. All of these alternatives are stable for $k \geq 2$.

55   A third option is the use of $Q_1 \times Q_1$ elements where both velocity and pressure use bi- or tri-linear shape functions. This combination of elements is not LBB-stable by default, but numerous stabilisation techniques – typically adding a pressure dependent term to the mass conservation equation – have been proposed in the literature (see e.g. Norburn and Silvester, 2001; Elman et al., 2014; Gresho et al., 1995). Herein, we will discuss in particular the variation by Dohrmann and Bochev (2004) that is simple to implement and does not involve any tunable parameter. This approach is used in the Rhea code (Burstedde

60   et al., 2009, 2013) in conjunction with Adaptive Mesh Refinement (AMR), allowing for the numerical solution of whole Earth models at high resolutions (Stadler et al., 2010; Alisic et al., 2012). Another example of the use of this method is the work of Leng and Zhong (2011), also using AMR, to study thermochemical mantle convection. Both the ELEFANT code with an application to the 3D thermal state of curved subduction zones (Plunder et al., 2018), and the GALE code (Moresi et al., 2012) with application to the 3D shapes of metamorphic core complexes (Le Pourhiet et al., 2012) or oceanic plateau subduction

65   (Arrial and Billen, 2013), use the stabilised $Q_1 \times Q_1$ method. Finally the ADELI code was coupled to a stabilised $Q_1 \times Q_1$ flow solver in the context of lithosphere-asthenosphere interaction studies (Cerpa et al., 2014, 2015, 2018).

     The availability of all of these options leads us to the main question of this paper: *Which element should one use in geodynamics computations based on the Stokes equations?*, or, in the absence of clear-cut conclusions, *Which ones should **not** be used?* On the face of it, this seems like a simple question: The consensus in the computational science community is that using

70   moderately high degree elements (say, $k = 3$ or $k = 4$) yields the best accuracy for a given computational effort (measured in CPU cycles), unless one wants to change the solver technology to use matrix-free methods where even higher polynomial degrees become more efficient. This conclusion is based on the higher convergence order of higher-degree methods, but balanced by the rapidly growing cost of matrix assembly and linear solver effort for higher-degree methods. On the other hand, the recommendation to use higher-degree methods is predicated on the assumption that the solution is smooth enough – say,

75   the velocity is in the Sobolev space H^{k+1} of functions that have, loosely speaking, at least $k + 1$ derivatives – so that one can actually achieve a convergence rate of $\mathcal{O}(h^k)$ in the energy norm and $\mathcal{O}(h^{k+1})$ in the L_2 norm where h is the mesh size. This assumption generally requires that all coefficients, such as density and viscosity, are sufficiently smooth on length scales resolvable by the mesh. This may not be the case in realistic geodynamics problems given that density and viscosity often depend discontinuously on the solution variables (velocity or strain rate, pressure, temperature, and compositional variables);

80   indeed, in many models, the viscosity may vary by orders of magnitude on short length scales.

     Such considerations put into question whether higher order methods are really worth the effort for actual geodynamics simulations. Given these divergent theoretical thoughts, the only way to resolve the question is by way of numerical comparisons. We have consequently extended ASPECT so that it can use all of the element combinations above, and will use these implementations in the comparisons in this paper.

85   **Goals of this paper.** Having outlined the conflict between the expected superiority of higher-degree elements for the Stokes equation on the one hand, and the expected lack of smoothness of solutions in realistic geodynamic cases, our goals in the paper are as follows:

1. To quantitatively compare the solution accuracy of the various options ($Q_1 \times P_0$, $Q_k \times Q_{k-1}$, $Q_k \times P_{-(k-1)}$ and stabilised $Q_1 \times Q_1$) using a variety of analytical benchmarks for which the exact solution is known. As we will see below, there

90   is little point working with $k > 2$ in geodynamics applications, and so the only cases we consider for Taylor-Hood-like elements are $Q_2 \times Q_1$ and $Q_2 \times P_{-1}$.

2. To extend these numerical comparisons to cases where it is known that the stabilised $Q_1 \times Q_1$ demonstrates problematic behaviour that may make it unusable in many practical situations. In particular, we will consider the case of buoyancy-driven flows.

95   3. To conclude our considerations by comparing the available options using a realistic geodynamical application. This will allow us to draw conclusions as to what element one might want to recommend for geodynamics applications.

While we have approached this study with an open mind and without a strong prior idea which element might be the best, let us end this introduction by noting that members of the crustal dynamics and mantle convection communities have occasionally expressed a dislike of the stabilised $Q_1 \times Q_1$ element for its inability to deal with large lithostatic pressures and free surfaces

100   absent special modifications of the formulation. For example, Arrial and Billen (2013) comment on the need to modify the physical description of the problem due to the stabilisation (with references replaced by ones listed at the end of this paper):

All the models were run with the open source code Gale. [...] Gale uses Q1–Q1 elements to describe the pressure and the velocity. However, this formulation is unstable and a slight compressible term is added in the divergence equation to stabilise it (Dohrmann and Bochev, 2004). Ideally, this term should be applied on the dynamic pressure

105   and not on the full pressure. To fix this, a hydrostatic term corresponding to the reference density and temperature profile, is subtracted from the full pressure and the body force vector.

Few other negative comments concerning the $Q_1 \times Q_1$ element appear on record in the published literature, although one can find the following quote in Lehmann et al. (2015) :

We do not consider the $Q_1 \times Q_1$/stab element (Dohrmann and Bochev, 2004; Bochev et al., 2006; Burstedde et al.,

110   2009), as stabilisation of this element is achieved by introducing an artificial compressibility that dominates for flows mainly driven by buoyancy variations (May et al., 2015). In geophysical flow models this yields unphysical pressure artifacts for cases where both the free surface of the Earth and mantle flow are considered, because the driving density contrast between cold sinking plates and the warmer surrounding Earth's mantle is much smaller than the density difference between rocks and air (Kaus et al., 2010; Popov and Sobolev, 2008; Mishin, 2011). In

115   our experience, this results in artificial "compaction" of the Earth's mantle if $Q_1 \times Q_1$/stab element is used, which makes them unsuitable for these purposes.

Indeed, our numerical experiments will encounter a similar issue, see Section 6.

We are not aware of any other significant publications in the geodynamics literature that specifically discuss the relative trade-offs between the elements we consider herein, specifically between the $Q_1 \times P_0$ and Taylor-Hood elements, and consequently

120   believe that our discussions here are useful for the community.

2 The governing equations

For the purpose of this paper, we are concerned with the accurate numerical solution of the incompressible Stokes equations:

$$-\nabla \cdot [2\eta\varepsilon(\boldsymbol{u})] + \nabla p = \rho\boldsymbol{g} \qquad \text{in } \Omega, \tag{1}$$

$$-\nabla \cdot \boldsymbol{u} = 0 \qquad \text{in } \Omega, \tag{2}$$

125 where η is the viscosity, ρ the density, $\boldsymbol{g}$ the gravity vector, $\varepsilon(\cdot)$ denotes the symmetric gradient operator defined by $\varepsilon(\boldsymbol{u}) = \frac{1}{2}(\nabla\boldsymbol{u} + \nabla\boldsymbol{u}^T)$, and $\Omega \subset \mathbb{R}^d, d = 2$ or 3 is the domain of interest. Both the viscosity η and the density ρ will, in general, be spatially variable; in applications, this is often through nonlinear dependencies on the strain rate $\varepsilon(\boldsymbol{u})$ or the pressure, but the exact reasons for the spatial variability are not of importance to us here: What matters is that these coefficients may vary strongly and on short length scales.

130   In applications, the equations above will be augmented by appropriate boundary conditions and will be coupled to additional and often time dependent equations, such as ones that describe the evolution of the temperature field or of the composition of rocks (see, for example, Schubert et al. (2001); Turcotte and Schubert (2012)). This coupling is also not of interest to us here.

3 Discretisation using finite element methods

3.1 Formulation and basic error estimates

135 For the comparisons we intend to make in this paper, equations (1)–(2) are discretised using the finite element method. A straightforward application of the Galerkin method yields the following finite-dimensional variational problem: *Find $\boldsymbol{u}_h \in \mathcal{U}_h, p_h \in \mathcal{P}_h$ so that*

$$(\varepsilon(\boldsymbol{v}_h), 2\eta\varepsilon(\boldsymbol{u}_h)) - (\nabla \cdot \boldsymbol{v}_h, p_h) = (\boldsymbol{v}_h, \rho\boldsymbol{g}),$$

$$-(q_h, \nabla \cdot \boldsymbol{u}_h) = 0, \tag{3}$$

for all test functions $\boldsymbol{v}_h \in \mathcal{U}_h, q_h \in \mathcal{P}_h$. Here, $(a,b) = \int_\Omega a(\boldsymbol{x})b(\boldsymbol{x}) \, dx$. For simplicity, we have omitted terms introduced
140 through the treatment of boundary conditions. The finite-dimensional, piecewise polynomial spaces $\mathcal{U}_h$ and P_h can be chosen in a variety of ways, as discussed in the introduction. In particular, if they are chosen as $\mathcal{U}_h = Q_k$ and $\mathcal{P}_h = Q_{k-1}$ – i.e., the Taylor-Hood element – then the discrete problem is known to satisfy the LBB condition and the solution is stable (Elman et al., 2014). Here, Q_s is the space of continuous functions that are obtained on each cell K of a mesh $\mathbb{T}$ by mapping polynomials of degree at most s in each variable from the reference cell $[0,1]^d$. Likewise, the problem is stable if one chooses $\mathcal{U}_h = Q_k$
145 and $\mathcal{P}_h = P_{-(k-1)}$ where now P_{-s} is the space of discontinuous functions obtained by mapping polynomials of *total* degree at most s from the reference cell. In both of these cases, we expect from fundamental theorems of the finite element method

(see, for example, Elman et al. (2014)) that the convergence rates are optimal, i.e., that the errors satisfy the relationships

$$\|\nabla(\boldsymbol{u} - \boldsymbol{u}_h)\|_{L_2} = \mathcal{O}(h^k),$$
$$\|\boldsymbol{u} - \boldsymbol{u}_h\|_{L_2} = \mathcal{O}(h^{k+1}),$$
$$\|p - p_h\|_{L_2} = \mathcal{O}(h^k), \tag{4}$$

150 where h is the maximal diameter over all cells in the mesh $\mathbb{T}$.

On the other hand, if one chooses $\mathcal{U}_h = Q_1$ and $\mathcal{P}_h = P_0$, i.e., the unstable $Q_1 \times P_0$ element with piecewise linear, continuous velocities and piecewise constant, discontinuous pressure, then the best convergence rates one can hope for would satisfy the following relationships, based solely on interpolation error estimates:

$$\|\nabla(\boldsymbol{u} - \boldsymbol{u}_h)\|_{L_2} = \mathcal{O}(h),$$
$$\|\boldsymbol{u} - \boldsymbol{u}_h\|_{L_2} = \mathcal{O}(h^2),$$
155 $$\|p - p_h\|_{L_2} = \mathcal{O}(h). \tag{5}$$

In practice, if the numerical solution shows pressure oscillations (see for instance Sani et al., 1981a, b), one will not even observe the rates shown above, but might in fact obtain a worse pressure convergence rate, for example $\|p - p_h\|_{L_2} = \mathcal{O}(h^{1/2})$.

Finally, if one uses $\mathcal{U}_h = Q_1$ and $\mathcal{P}_h = Q_1$, then this unstable element combination can be made stable if one replaces the discrete formulation (3) by the following, stabilised version due to Dohrmann and Bochev (2004):

$$(\varepsilon(\boldsymbol{v}_h), 2\eta\varepsilon(\boldsymbol{u}_h)) - (\nabla \cdot \boldsymbol{v}_h, p_h) = (\boldsymbol{v}_h, \rho\boldsymbol{g}),$$
160 $$(q_h, \nabla \cdot \boldsymbol{u}_h) - \left((I - \pi_0)q_h, \frac{1}{\eta}(I - \pi_0)p_h\right) = 0. \tag{6}$$

Here, I is the identity operator and π_0 is the projection onto piecewise constant functions – i.e., $\pi_0 f$ is the function that on each cell is equal to the mean value of f on that cell. For this element, the rates one might hope for are as follows (see again Dohrmann and Bochev (2004)):

$$\|\nabla(\boldsymbol{u} - \boldsymbol{u}_h)\|_{L_2} = \mathcal{O}(h),$$
$$\|\boldsymbol{u} - \boldsymbol{u}_h\|_{L_2} = \mathcal{O}(h^2),$$
165 $$\|p - p_h\|_{L_2} = \mathcal{O}(h). \tag{7}$$

Dohrmann and Bochev (2004) report that for some test cases, one might in fact obtain $\|p - p_h\|_{L_2} = \mathcal{O}(h^t)$ with $t \approx 1.5$, though it is not clear whether this rate can be obtained for all possible applications. We also observe this improved rate in one of our benchmarks in Section 5.

3.2   A closer look at the error estimates

170 A comparison of (4) with (5) and (7) would suggest that the Taylor-Hood element can obtain substantially better rates of convergence if one only chooses the polynomial degree k large enough.

However, this is an incomplete understanding because the $\mathcal{O}(h^m)$ notation hides the fact that the constants in this behaviour depend on the solution. More specifically, a complete description of the error behaviour would replace (4) by the following statement: There exist constants $C_1, C_2, C_3 < \infty$ so that

$$\|\nabla(\boldsymbol{u} - \boldsymbol{u}_h)\|_{L_2} \le C_1 \, h^k \, \|\nabla^{k+1}\boldsymbol{u}\|_{L_2},$$

$$\|\boldsymbol{u} - \boldsymbol{u}_h\|_{L_2} \le C_2 \, h^{k+1} \, \|\nabla^{k+1}\boldsymbol{u}\|_{L_2},$$

$$\|p - p_h\|_{L_2} \le C_3 \, h^k \, \|\nabla^k p\|_{L_2}. \tag{8}$$

The validity of these statements clearly depends on the solution to be regular enough so that $\nabla^{k+1}\boldsymbol{u}$ and $\nabla^k p$ actually exist and are square integrable – in other words, that $\boldsymbol{u} \in H^{k+1}$ and $p \in H^k$. On the other hand, all that is guaranteed by the existence theory for partial differential equations is that $\boldsymbol{u} \in H^1$ and $p \in L_2 = H^0$; any further smoothness should only be expected if, for example, the domain Ω is convex, and if viscosity η and right hand side $\rho\boldsymbol{g}$ are also smooth. Indeed, this is the case for many artificial benchmarks where these functions are chosen a priori; on the other hand, in "realistic" geodynamics applications, one might expect η and ρ to be discontinuous at phase boundaries, and potentially vary widely. In such cases, one needs to accept that the solutions only satisfy $\boldsymbol{u} \in H^q$ and $p \in H^{q-1}$ with $q \ge 1$ but possibly $q < k + 1$. Numerical analysis predicts that in such cases, the best case rates in (8) will be replaced by the following:

$$\|\nabla(\boldsymbol{u} - \boldsymbol{u}_h)\|_{L_2} \le C_1 \, h^{\min\{q-1,k\}} \, \|\nabla^{\min\{q,k+1\}}\boldsymbol{u}\|_{L_2},$$

$$\|\boldsymbol{u} - \boldsymbol{u}_h\|_{L_2} \le C_2 \, h^{\min\{q,k+1\}} \, \|\nabla^{\min\{q,k+1\}}\boldsymbol{u}\|_{L_2},$$

$$\|p - p_h\|_{L_2} \le C_3 \, h^{\min\{q-1,k\}} \, \|\nabla^{\min\{q-1,k\}}p\|_{L_2}. \tag{9}$$

Similar considerations apply for the $Q_1 \times P_0$ and the stabilised $Q_1 \times Q_1$ combinations, where a closer examination yields the following rates that would replace (5) and (7):

$$\|\nabla(\boldsymbol{u} - \boldsymbol{u}_h)\|_{L_2} \le C_1 \, h^{\min\{q-1,1\}} \, \|\nabla^{\min\{q,2\}}\boldsymbol{u}\|_{L_2},$$

$$\|\boldsymbol{u} - \boldsymbol{u}_h\|_{L_2} \le C_2 \, h^{\min\{q,2\}} \, \|\nabla^{\min\{q,2\}}\boldsymbol{u}\|_{L_2},$$

$$\|p - p_h\|_{L_2} \le C_3 \, h^{\min\{q-1,1\}} \, \|\nabla^{\min\{q-1,1\}}p\|_{L_2}. \tag{10}$$

In other words, we will only benefit from the added expense of the Taylor-Hood element with $k \ge 2$ if the solution is sufficiently smooth, namely if at least $q > k \ge 2$. The question whether indeed $q > 2$ for a given situation is one of PDE theory and difficult to answer in general without using particular knowledge of η, $\rho\boldsymbol{g}$, and Ω. On the other hand, one can observe convergence rates experimentally for a number of cases of interest, and so in some sense, it would be a legitimate question to ask "*What is the regularity index q of typical solutions in geodynamics applications?*" At the same time, this requires careful convergence studies on problems that are typically quite challenging to solve already on any reasonable mesh, let alone several further refined ones. As a consequence, we can not answer this question in the generality stated above. Instead, we will below approach it by considering a number of benchmarks that illustrate typical features of geodynamic settings in an abstracted way (in Section 5), followed by a model application (in Section 6).

4   Comments about the use of the $Q_1 \times Q_1$ element in geodynamics computations

Before delving into the details of numerical experiments, let us consider one other theoretical aspect. An interesting complication of geodynamics simulations compared to many other applications of the Stokes equations is that the hydrostatic component of the pressure is often vastly larger than the dynamic pressure, even though only the dynamic component is responsible for driving the flow. As we will discuss in the following, this has no importance when using the $Q_1 \times P_0$ or the Taylor-Hood elements, but turns out to be rather inconvenient when using a stabilised formulation that contains an artificial compressibility term. This issue is also mentioned in the quote from Arrial and Billen (2013) reproduced in the introduction, and in May et al. (2015).

To illustrate the issue, consider the force balance equation (1). We can split the pressure into hydrostatic and dynamic components, $p = p_s + p_d$ where we define the hydrostatic pressure via the relationship

$$\frac{\partial}{\partial z} p_s = \rho_{\text{ref}}(z) g_z(z), \tag{11}$$

coupled with the normalisation that $p_s = 0$ at the top of the domain. In defining p_s this way, we have made the assumption that the vertical component g_z of the gravity vector dominates its other components. Furthermore, we have introduced a *reference density* ρ_{ref} that somehow reflects a depth-dependent profile. As we will discuss below, there is really no unique or accepted way to define this profile, though one should generally think of it as capturing the bulk of the three-dimensional variation in the density via a one-dimensional function.

By splitting the pressure in this way, (1) can then be rewritten as follows:

$$-\nabla \cdot [2\eta \epsilon(\boldsymbol{u})] + \nabla p_d = \rho \boldsymbol{g} - \rho_{\text{ref}} g_z \boldsymbol{e}_z \qquad \text{in } \Omega.$$

Since this is the only equation in which the pressure appears, it is obvious that the velocity field so computed is the same whether or not one uses the original formulation solving for $\boldsymbol{u}, p$, or the one solving for $\boldsymbol{u}, p_d$. More concisely, the observation shows that *the velocity field so computed does not depend on how one chooses the reference density ρ_{ref}*. The original formulation is recovered by using the simplest choice, $\rho_{\text{ref}} = 0$. As a consequence, many geodynamics codes use formulations that only compute the dynamic pressure p_d, using a reference density $\rho_{\text{ref}}(z)$. Importantly however, there is no canonical way for this definition: one might choose a constant reference density, a depth-dependent adiabatic profile, or one computed at each time step by laterally averaging the current three-dimensional density field $\rho(x, y, z, t)$; each of these options – and likely more – have been used in numerical simulations one can find in the literature. In any case, pressure-dependent coefficients such as the density or viscosity are then evaluated by using $p_s + p_d$ where p_d is computed as part of the solution of the Stokes problem and p_s is the hydrostatic pressure defined by (11) using the particular choice of reference density used by a code. On the other hand, the ASPECT code notably *always* computes the full pressure instead of splitting it in hydrostatic and dynamic components (see the discussion in Kronbichler et al. (2012)), corresponding to the particular choice $\rho_{\text{ref}} = 0$.

The problem with the stabilised $Q_1 \times Q_1$ formulation – different from the use of the other element choices – is that the velocity field computed from the Stokes solution is *not* independent of the choice of the reference density. This is because the

Solid Earth
Discussions

Open Access

EGU

mass conservation equation is modified by the stabilisation term and – in the simple case of a constant viscosity – reads

$$-\nabla \cdot \boldsymbol{u} - \frac{1}{\eta}\Pi p_d = 0. \tag{12}$$

Here, $\Pi = (I - \pi_0)$ is the operator that corresponds to the stabilisation term in (6).[1]

235   The point of these considerations is that different choices of ρ_{ref} (including the choice $\rho_{\text{ref}} = 0$ that leads to the original formulation) do have an effect here because they lead to different $p_d = p - p_s$ for which Πp_d is different: that is, the amount of artificial compressibility depends on the splitting of the pressure into static and dynamic pressures. In other words, *the discretisation errors $\|\boldsymbol{u} - \boldsymbol{u}_h\|_{L_2}$ and $\|\nabla(\boldsymbol{u} - \boldsymbol{u}_h)\|_{L_2}$ discussed in the previous section will in general depend on the choice of the reference density profile*, and the latter will need to be carefully defined in order to lead to acceptable error levels. As

240   we will show in the benchmarking section, the specific choice of ρ_{ref} in fact has a rather large effect. This is in line with the previously quoted comments in Arrial and Billen (2013).

    Let us end this section by commenting on two aspects why this issue may not be as relevant in other contexts in which stabilised formulations have been used. First, in many important applications of the Stokes equations, the flow is not driven by buoyancy effects but by inflow and outflow boundary conditions (e.g. Turek, 1999; Zienkiewicz and Taylor, 2002). Indeed, in

245   those conditions both the density and the gravity vector is generally considered spatially constant, and the choice of reference density and hydrostatic pressure is then obvious and unambiguous. In these cases, computations are *always* performed with only the dynamic pressure because the hydrostatic pressure does not enter the problem at all except in the rare cases of fluids with pressure-dependent viscosities.

    Second, while we have here considered the stabilisation first introduced in Dohrmann and Bochev (2004), earlier stabilised

250   formulations used a pressure Laplacian in place of the operator Π above. (See, for example, Brezzi and Pitkäranta (1984) or the variation in Silvester and Kechkar (1990), as well as the analysis in Bochev et al. (2006).) That is, instead of (12) they used a formulation of the form

$$-\nabla \cdot \boldsymbol{u} - ch^2 \Delta p = 0, \tag{13}$$

where c is a tuning parameter that also incorporates the viscosity. If one uses this formulation for cases in which the reference

255   density is chosen as a function that is constant in depth – as was often done in earlier mantle convection codes considering the Boussinesq approximation – and if one computes in a Cartesian box with a constant gravity vector $\mathbf{g} = g\mathbf{e}_z$, then p_s is a linear function, and consequently $\Delta p_s = 0$. In other words, $\Delta p = \Delta(p - p_s) = \Delta p_d$, which implies that the computed velocity field again did not depend on the exact choice of ρ_{ref} as long as it was chosen constant. This property does not hold for the formulation of Dohrmann and Bochev because $\Pi p \neq \Pi(p - p_s) = \Pi p_d$ for linear pressures p_s because $\Pi p_s \neq 0$: Π subtracts

260   from p_s the average value on each cell, leaving a piecewise linear, discontinuous function.

    Of course, whether one uses the Dohrmann-Bochev formulation (12) or the addition of a pressure Laplace as in (13), the formulation is consistent. That is, as the mesh size h goes to zero, the added stabilisation term also goes to zero. In the limit,

---

[1]To arrive at this form for the operator, one needs to re-write (6) using $\left((I - \pi_0)q_h, \frac{1}{\eta}(I - \pi_0)p_h\right) = \left(q_h, \frac{1}{\eta}(I - \pi_0)^*(I - \pi_0)p_h\right)$ where the asterisk denotes the adjoint operator. One then shows $(I - \pi_0)^* = (I - \pi_0)$ and finally that $\Pi = (I - \pi_0)^2 = I - \pi_0$, which follows by recalling that projection operators are idempotent.

Solid Earth
Discussions

Open Access

the numerical solution therefore satisfies the original mass conservation equation. In other words, the *limit* is independent of the choice of ρ_{ref}, even though the solutions on a finite mesh are not.

265 ## 5 Numerical results for artificial benchmarks

In this section, let us present computational results for three analytical problems and a buoyancy-driven flow community benchmark. While the first of these (Section 5.1) is simply used to establish the best convergence rates one can hope for in the case of smooth solutions, the remaining test cases were chosen because they illustrate aspects of what we think how "typical" solutions of geodynamic applications look like in an abstracted, controlled way. In particular, the "SolCx" benchmark in
270 Section 5.2 demonstrates features of solutions in which the mesh can be aligned with sharp features in the viscosity, and the "SolVi" benchmark in Section 5.3 does so in the more common case where the mesh can not be aligned. Finally, the "sinking block" case in Section 5.4 shows a buoyancy-driven situation in which all of the discussions of the previous section on the choice of a reference density will come to play. All of these cases are simple enough that we know (quantitative or qualitative features of) the solution to sufficient accuracy to investigate convergence rigorously.

275 While these benchmarks provide us with insight that allows us to *conjecture* which elements may or may not work in practical application, they still are just abstract benchmarks. As a consequence, we will consider an actual geodynamic application in Section 6.

All models are run with the ASPECT code. We have limited ourselves to two-dimensional cases as we do not expect that three-dimensional models would shed any more light on the reached conclusions. Although ASPECT is built for adaptive mesh
280 refinement (AMR), we have chosen not to use this feature in order to reflect that the majority of existing codes use structured meshes.

5.1 The Donea & Huerta benchmark

Let us start our numerical experiments with the simple 2D benchmark presented in Donea and Huerta (2003). The exact definition involves lengthy formulas not worth repeating here, but in short it consists of the following ingredients: (i) The
285 domain is a unit square; (ii) the viscosity and density are set to 1; (iii) velocity and pressure fields are chosen to correspond to smooth polynomials describing circular flow with no-slip boundary conditions. We then choose an (unphysical) gravity vector field that produces these velocity and pressure fields. This set up produces the smooth solution shown in Fig. 1 for which we would expect that the higher-order Taylor-Hood element is highly accurate.

We verify this in Fig. 2 for the four element choices of interest in this work: $Q_1 \times P_0$, stabilised $Q_1 \times Q_1$, $Q_2 \times Q_1$, $Q_2 \times P_{-1}$.
290 Looking at the velocity error, we recover a cubic convergence rate ($q = 3$) for the $Q_2 \times Q_1$ and $Q_2 \times P_{-1}$ elements, and a quadratic convergence rate ($q = 2$) for those choices using the Q_1 elements for the velocity. The pressure error is of linear rate for the $Q_1 \times P_0$ element and of quadratic rate for the $Q_2 \times Q_1$ and $Q_2 \times P_{-1}$ elements. All of these are as expected. For the stabilised $Q_1 \times Q_1$, we obtain the better-than-expected rate of 1.5 already mentioned in Dohrmann and Bochev (2004), see also Section 3.
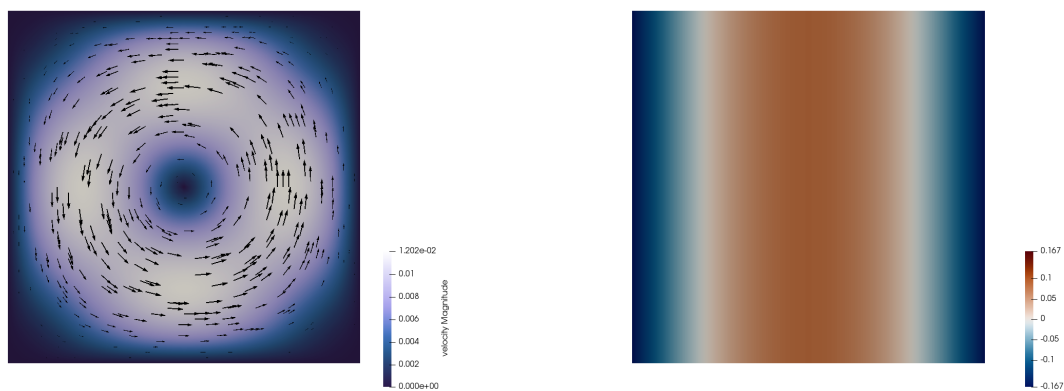
Figure 1. Donea & Huerta benchmark. Velocity (left) and pressure (right) fields obtained on a 32×32 mesh with $Q_2 \times Q_1$ elements.

Fig. 3 shows the root mean square velocity as a function of the mesh size as obtained with the four elements in question. Again, the second-order elements are more accurate.

These results are not surprising: The solution is smooth, and consequently one would expect to obtain optimal order convergence in all cases. One can carry out similar experiments for the SolKz benchmark (Zhong, 1996), which also has a smooth solution; we have obtained identical error convergence rates.

Finally, we also investigate the cost associated with solving this problem using the various elements. Fig. 3 shows the number of outer iteration of the Stokes solver as a function of the mesh size. This number is nearly constant with increasing resolution for the stable or stabilised elements while it becomes exceedingly large for the unstable $Q_1 \times P_0$ element, reflecting the fact that lack of LBB stability corresponds to the smallest eigenvalue of the system matrix tending to zero – and thereby driving the condition number to infinity. Indeed, our linear solver does not converge in the 1000 iterations we chose as a limit for the smallest mesh sizes.

5.2 The SolCx benchmark

The SolCx benchmark is a common benchmark found in many geodynamical papers (e.g. Zhong, 1996; Duretz et al., 2011; Kronbichler et al., 2012; Thielmann et al., 2014). It uses a discontinuous viscosity profile with a large jump in the viscosity value along the middle of the domain, resulting in a discontinuous pressure field. The domain is a unit square, boundary conditions are free-slip on all edges, and the gravity vector points downwards with $|\boldsymbol{g}| = 1$. The density for SolCx is given by $\rho(x, y) = \sin(\pi y) \cos(\pi x)$ and the viscosity field is such that

$$
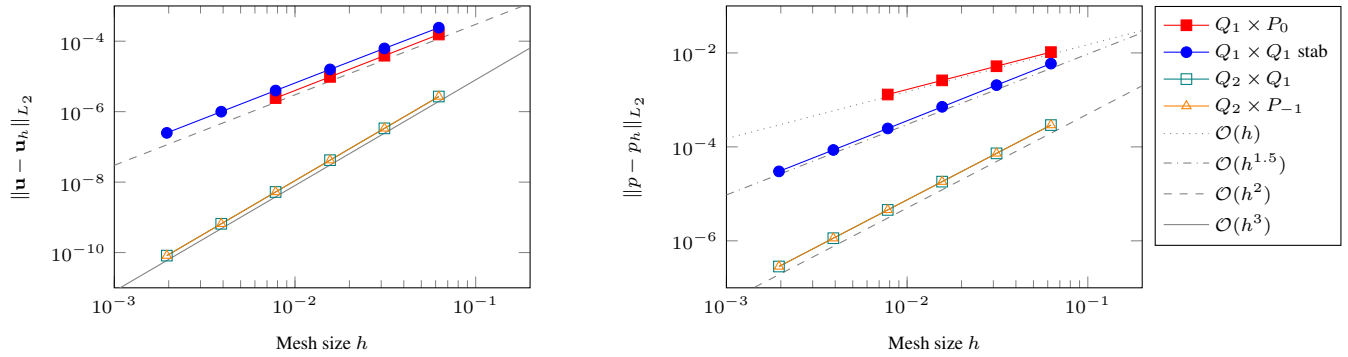\eta(x, y) = \begin{cases} 1, & \text{if} \quad 0 \leq x \leq 0.5 \\ 10^6 & \text{if} \quad 0.5 < x \leq 1. \end{cases}
$$

Figure 2. Donea & Huerta benchmark. Error convergence as a function of the mesh size h. Left: Velocity error $||\mathbf{u} - \mathbf{u}_h||_{L_2}$. Right: Pressure error $||p - p_h||_{L_2}$. The two leftmost points are missing for $Q_1 \times P_0$ since the solver failed to converge; the data points for $Q_2 \times Q_1$ and $Q_2 \times P_{-1}$ are on top of each other.
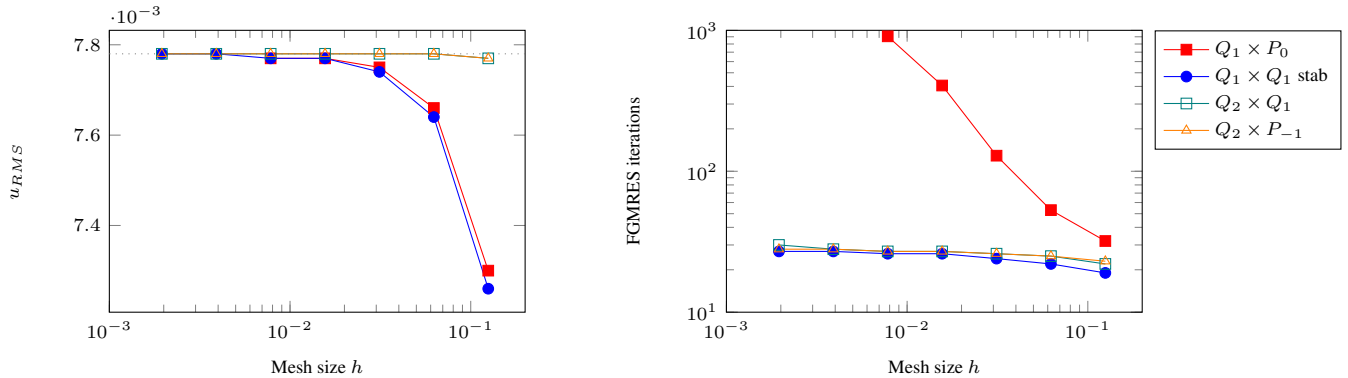

Figure 3. Donea & Huerta benchmark. Left: Root mean square velocity as a function of the mesh size h. The dotted line is the analytical value. Right: Number of FGMRES solver iterations as a function of the mesh size h.

We show the velocity and pressure fields in Fig. 4. The discontinuous jump of the viscosity field by a factor of 10^6 results in separate convective cells on the left and right sides of the domain, though with vastly different strengths. The pressure also
315 reflects this disjoint behaviour.

As in the Donea & Huerta benchmark, we compute the velocity and pressure error convergence for all four elements. Those are shown in Fig. 5. As documented in Kronbichler et al. (2012), the second order element with discontinuous pressure $Q_2 \times P_{-1}$ performs better (pressure error convergence is $\mathcal{O}(h^2)$) than its continuous pressure counterpart $Q_2 \times Q_1$ (convergence is only $\mathcal{O}(h^{1/2})$, but the better convergence order with the discontinuous pressure can only be obtained if the discontinuity
320 in the viscosity is aligned with cell boundaries – which is the case here. Also of interest here is the fact that the $Q_1 \times P_0$ outperforms the $Q_1 \times Q_1$ element for both velocity and pressure. All of these observations are readily explained by the fact
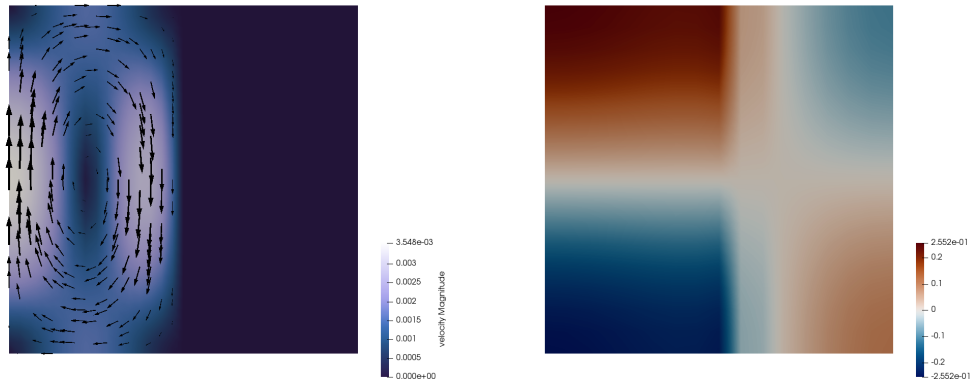
Figure 4. SolCx benchmark. Velocity (left) and pressure (right) fields obtained on a mesh with a resolution of 32×32 grid with the $Q_2 \times Q_1$ element.
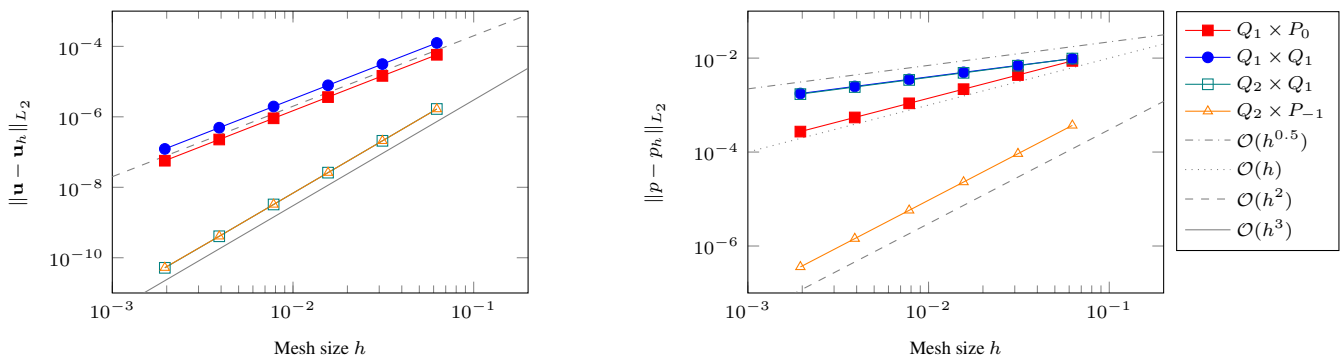

Figure 5. SolCx benchmark. Error convergence as a function of the mesh size h. Left: velocity error; right: pressure error.

that a discontinuous pressure can only be approximated well when using discontinuous pressure elements with cell interfaces aligned with the discontinuity in the viscosity.

5.3 The SolVi (circular inclusion) benchmark

325   The SolCx benchmark in the previous section allows for aligning mesh interfaces with the discontinuity in the viscosity. This is an artificial situation that will, in general, not happen in actual geodynamics applications where the interfaces between materials may be at arbitrary locations and orientations in the domain, and may also move with time. An example is the simulation of a cold, subducting slab (with correspondingly large viscosity) surrounded by hot, low-viscosity mantle material. Consequently, it is worth considering a situation in which it is impractical to align mesh and viscosity interfaces. This is done

330   by the SolVi inclusion benchmark which solves a problem with a viscosity that is discontinuous along a circle. This in turns leads to a discontinuous pressure along the interface which is difficult to represent accurately. Using the regular meshes used by
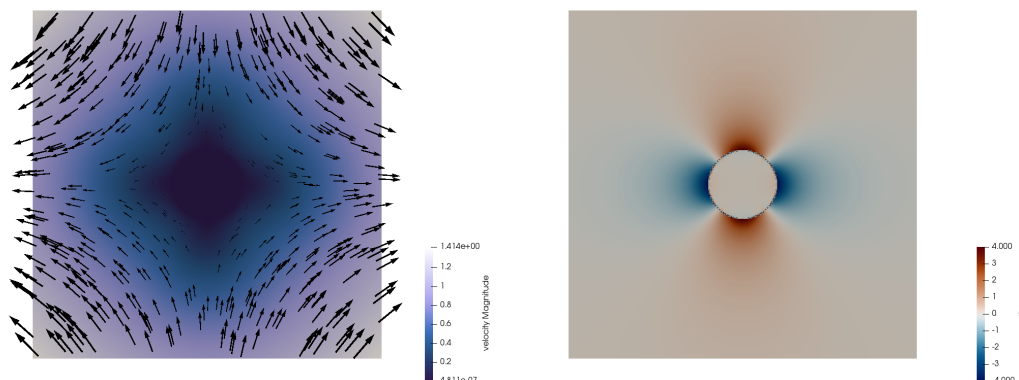
Figure 6. SolVi benchmark with inclusion of radius 0.2. Velocity (left) and pressure (right) fields obtained on a 256×256 mesh using $Q_2 \times Q_1$ elements.

a majority of codes, the discontinuity in the viscosity and pressure then never aligns with cell boundaries. Even though ASPECT can use arbitrary, unstructured meshes (and can also used curved cell edges), we will honor the setup of this benchmark by only considering regular meshes.

335   Schmid and Podlachikov (2003) derived a simple analytical solution for the pressure and velocity fields for such a circular inclusion under simple shear and this benchmark is showcased in many publications (Deubelbeiss and Kaus, 2008; Suckale et al., 2010; Duretz et al., 2011; Kronbichler et al., 2012; Gerya et al., 2013; Thielmann et al., 2014). The velocity and pressure fields are shown in Fig. 6.

A characteristic of the analytic solution is that the pressure is zero inside the inclusion, while outside it follows the relation

$$
340 \quad p = 4\dot{\epsilon}\frac{\eta_m(\eta_i - \eta_m)}{\eta_i + \eta_m}\frac{r_i^2}{r^2}\cos(2\theta) \tag{14}
$$

where $\eta_i = 10^3$ is the viscosity of the inclusion and $\eta_m = 1$ is the viscosity of the background medium, $r = \sqrt{x^2 + y^2}$ and $\theta = \arctan(y/x)$, and $\dot{\epsilon} = 1$ is the applied strain rate if one were to extend the domain to infinity. The formula above makes it clear that the pressure is discontinuous along the perimeter of the disk, with the jump largest at $\theta = 0, \pm\frac{\pi}{2}, \pi$.

Deubelbeiss and Kaus (2008) thoroughly investigated this problem with various numerical methods (FEM, FDM), with and
345   without tracers, and conclusively showed how various schemes of averaging the density and viscosity lead to different results. Heister et al. (2017) also come to this conclusion, and also considered how averaging the coefficient on each cell affects the number of iterations necessary to solve the linear systems. We repeat these experiments here but with our larger set of different elements. Specifically, results obtained with no averaging inside the element ('No'), arithmetic averaging ('Arith'), geometric averaging ('Geom') and harmonic averaging ('Harm') are shown in Fig. 7. We see that (i) all four elements show the same rate
350   of convergence: $\mathcal{O}(h)$ for velocity errors and $\mathcal{O}(h^{0.5})$ for pressure errors; (ii) harmonic averaging always yields lower errors, validating the findings of Heister et al. (2017); (iii) the number of iterations in the Stokes solver is the lowest for the stabilised $Q_1 \times Q_1$ element; and (iv) this number is not strongly affected by the method of averaging (with the exception of the $Q_2 \times P_{-1}$
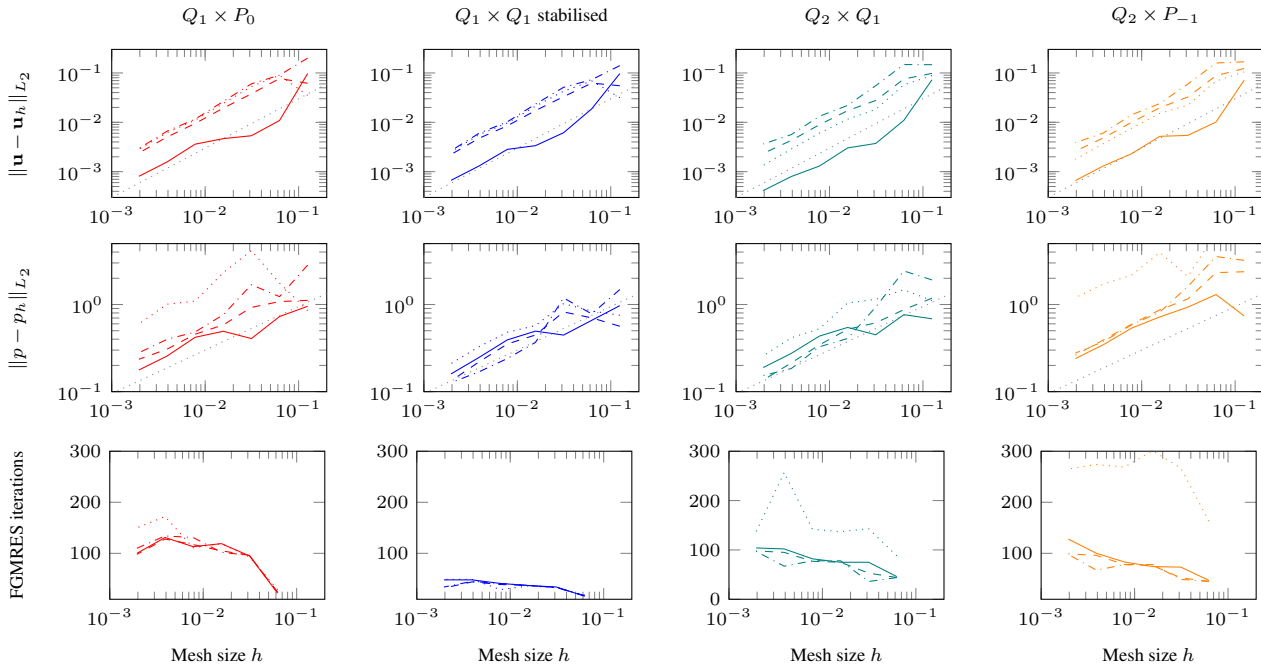
14

Figure 7. SolVi benchmark. Left to right: $Q_1 \times P_0$, stabilised $Q_1 \times Q_1$, $Q_2 \times Q_1$ and $Q_2 \times P_{-1}$. Top to bottom: Velocity error, pressure error, and number of FGMRES iterations for the Stokes solve. The individual lines in each graph correspond to different ways of averaging coefficients on each cell: dotted lines use the correct, unaveraged, values of coefficients at each quadrature point; dash-dotted lines compute the arithmetic average of the values at the quadrature points on a cell and use the average for all quadrature points; dashed lines use the geometric average; solid lines use the harmonic average. The gray dotted line in the first two rows indicates $\mathcal{O}(h)$ convergence for velocity and $\mathcal{O}(h^{0.5})$ for pressure.

element). The observation that the none of the elements reach their optimal convergence rate also supports our decision, briefly mentioned in the "Goals of this paper" part of the Introduction, to not further investigate higher-order Taylor-Hood elements

355 $Q_k \times Q_{k-1}$ or $Q_k \times P_{-(k-1)}$ with $k > 2$: We know from experiments such as the current one that these elements will not yield better convergence orders despite their additional cost.

Since harmonic averaging yields the lowest errors we select this averaging and now turn to the pressure field for all elements as shown in Fig. 8. We find that the recovered pressures on the line $y = 1$ follow the analytical solution outside of the inclusion but are less accurate inside the inclusion where it should be identically zero (Fig. 9).

5.4 The sinking block

360

As discussed in Section 4, the stabilised $Q_1 \times Q_1$ element is sensitive to the choice of a reference density profile as not only the computed pressure, but also the computed velocity field depends on this choice. This is only relevant for buoyancy-driven flows, but because none of the benchmarks shown previously are driven by buoyancy effects in the presence of a background
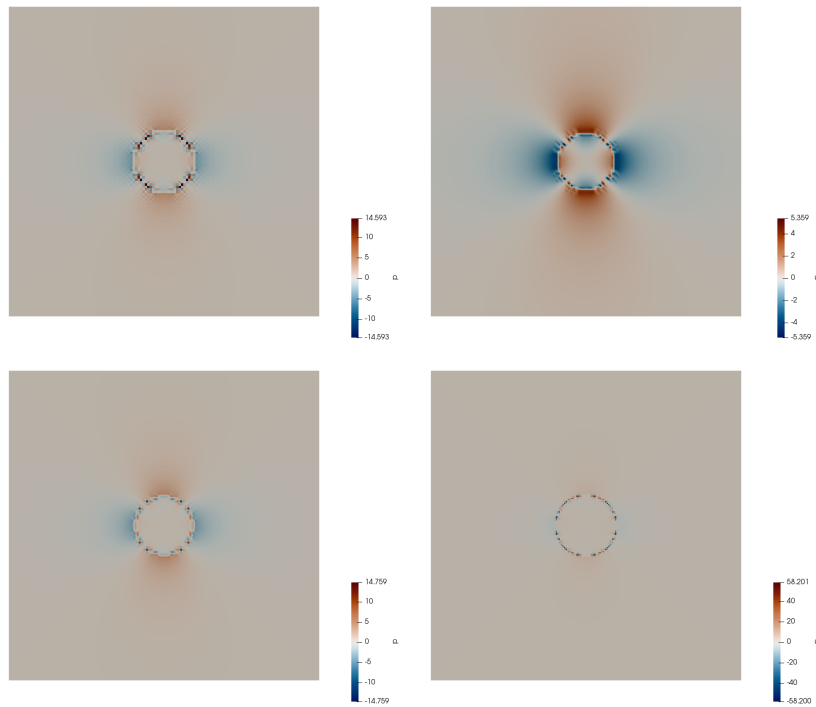
Figure 8. SolVi benchmark. Pressure field for the $Q_1 \times P_0$, stabilised $Q_1 \times Q_1$, $Q_2 \times Q_1$ and $Q_2 \times P_{-1}$ elements respectively from left to right and top to bottom, at resolution 128x128, with no averaging. Note the different color scales, illustrating the differing size of over- and undershoots for the different discretisations.
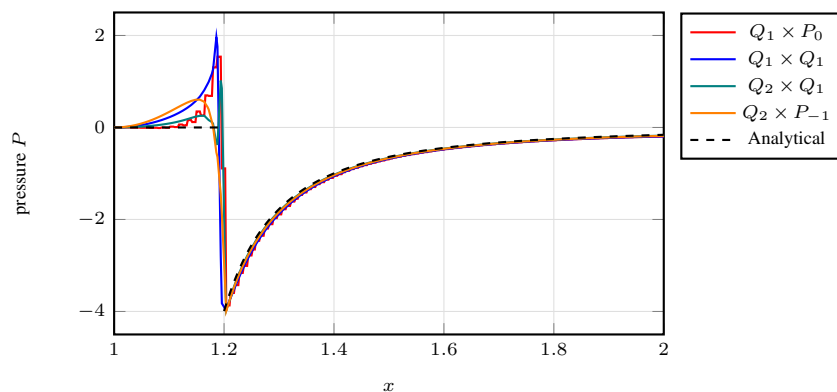

Figure 9. SolVi benchmark. Pressure on the horizontal ray starting from the center of the inclusion at $x = 1$.

lithostatic pressure to any significant degree, let us next consider a setup in which this is the dominant effect. To this end,
we perform an experiment based on a benchmark similar or identical to the ones presented in May and Moresi (2008), Gerya
(2010), Thieulot (2011) and Schuh-Senlis et al. (2020).

It consists of a two-dimensional 512×512km domain filled with a fluid (the "mantle") of density $\rho_1 = 3200$kg m^{-3} and viscosity $\eta_1 = 10^{21}$Pa s. A square block of size 128×128km is placed in the domain and is centered at location (x_c, y_c)=(256km,
384km) so as to insure that its sides align with cell boundaries at all resolutions, avoiding cases where the quadrature within one
element correspond to different density or viscosity values. It is filled with a fluid of density $\rho_2 = \rho_1 + \delta\rho$ and viscosity η_2. The
gravity vector points downwards with $|\boldsymbol{g}| = 10$m s^{-2}. Boundary conditions are free slip on all sides. The pressure nullspace
is removed by enforcing $\int_\Omega p \, \mathrm{d}V = 0$ and only one time step is carried out. The benchmark then solves for the instantaneous
pressure and velocity field for this setup.

In a geodynamical context, the block could be interpreted as a detached slab ($\delta\rho > 0$) or a plume head ($\delta\rho < 0$). As such its
viscosity and density can vary (a cold slab has a higher effective viscosity than the surrounding mantle while it is the other way
around for a plume head). The block density difference $\delta\rho$ can then vary from a few to several hundred kg m^{-3} to represent a
wide array of scenarios. As shown in Appendix A.2 of Thieulot (2011), one can independently vary η_1, ρ_2, η_2, and measure
$|v_z|$ for each combination: the quantity $\nu = |v_z|\eta_1/\delta\rho$ is then found to be a simple function of the ratio $\eta^\star = \eta_2/\eta_1$: at high
enough mesh resolution all data points collapse onto a single line.

In the following, we will denote by "Method #1" the approach where we do calculations with the density field as specified
above. "Method #2" consists of a 'reduced' density field from which the quantity ρ_1 has been uniformly removed so that the
block has a density $\delta\rho$ while the surrounding fluid has zero density. As discussed above, the two choices will result in different
pressure, but the same velocity fields.

We have carried out measurements for all four elements with $\eta^\star \in [10^{-4} : 10^6]$, and $\delta\rho/\rho_1 \in \{0.25\%, 1\%, 4\%\}$ corresponding to $\delta\rho \in \{8, 32, 128\}$kg m^{-3}. Results for $\nu = f(\eta^\star)$ for all elements, the three block density values, and five different mesh
resolutions are shown in Fig. 10 for the two methods.

When using the full density, we see that all elements, with the exception of the stabilised $Q_1 \times Q_1$ element, yield results
which align on a single curve on the plots once sufficient resolution is reached. We find that measurements pertaining to a given
resolution but different $\delta\rho$ are always collapsed onto a single line. Worth noticing is the $Q_2 \times P_{-1}$ element whose results seem
to be the least resolution dependent. On the other hand the stabilised $Q_1 \times Q_1$ element yields very anomalous results which are
orders of magnitude off at all resolutions, especially for $\eta_1/\eta_2 \gg 1$. In addition, we find that for this element, the value of $\delta\rho$
strongly affects the measurements, as expected based on the discussions in Section 4; as a result, the curves for the same mesh
resolution but different $\delta\rho_2$ no longer coincide (see Fig. 10b).

When reduced densities are used results are unchanged for the stable elements (only $Q_2 \times Q_1$ results are shown in Fig. 10e),
and the results for the stabilised $Q_1 \times Q_1$ results are substantially improved. For values $\eta_1/\eta_2 < 1$ we see that all results align
on the expected curve but this is far from true for $\eta_1/\eta_2 \gg 1$ even at high resolution.

In Fig. 11 we show the velocity field in the case $\eta^\star = 10^{-4}$ (i.e. the viscosity of the block is 10,000 times smaller than
the surrounding mantle) and $\delta\rho = 8$kg m^{-3}. When the $Q_2 \times Q_1$ element is employed in conjunction with Method 1 we see in

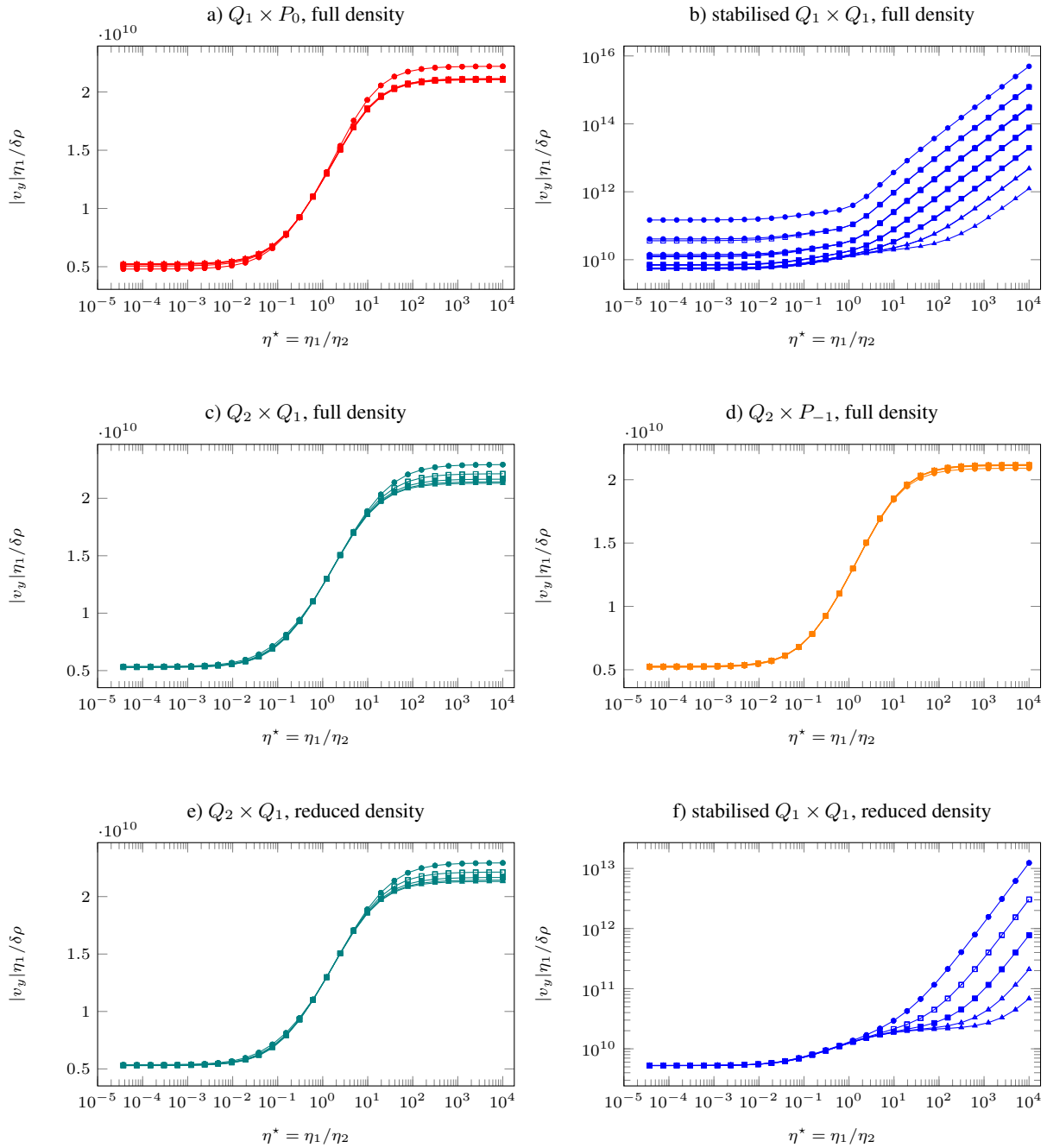**Figure 10.** Sinking block benchmark. a,b,c,d) $\nu = |v_z|\eta_1/\delta\rho$ as a function of $\eta^\star = \eta_2/\eta_1$ as obtained with with the four elements with full density; e,f) same with reduced density for only two element types. Legend: • 16×16 resolution, □ 32×32 resolution, ■ 64×64 resolution, △ 128×128 resolution, ▲ 256×256 resolution. Colors represent the element used. For each mesh resolution, we show separate curves for $\delta\rho/\rho_1 \in \{0.25\%, 1\%, 4\%\}$; for all but the stabilised $Q_1 \times Q_q$ element, these curves coincide. Note the different y-axis used for the stabilised $Q_1 \times Q_1$ element in b) and f).
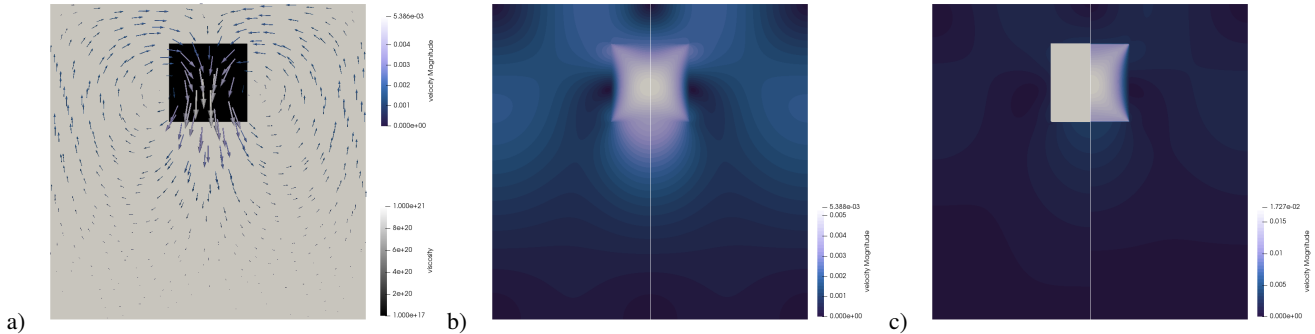
Figure 11. Sinking block benchmark with $\delta\rho/\rho = 0.25\%$ and $\eta^\star = 10^4$ on 256×256 element mesh. a) Viscosity and velocity field. b) Velocity field obtained with $Q_2 \times Q_1$ element (left of vertical white line) and $Q_2 \times P_{-1}$ element (right of vertical line) both using full density; c) Velocity field obtained with stabilised $Q_1 \times Q_1$ with full density (left) and stabilised $Q_1 \times Q_1$ with reduced density (right).

Fig. 11a that the velocity field is strongest inside the block with a maximum value of about $5\mathrm{mm}\,\mathrm{yr}^{-1}$ in its center. We see

400 that the $Q_2 \times Q_1$ and $Q_2 \times P_{-1}$ elements yield near identical results (Fig. 11b) so we consider this to be the correct solution of the physical experiment. The same setup with the stabilised $Q_1 \times Q_1$ (left half of Fig. 11c) yields a velocity field that is also maximal in the middle of the block but nearly 1000 times larger in amplitude. If we now switch to Method 2 (right half of Fig. 11c) the amplitude of the velocity is reduced by two orders of magnitude but it is still much too large compared to the true solution.

405   These observations illustrate the unreliable nature of the results obtained with stabilised $Q_1 \times Q_1$ elements in the context of buoyancy-driven flows. Looking at Fig. 10f we see that increasing the resolution to 512×512 or 1024×1024 would probably yield the expected curve but such resolutions are intractable in three dimensions and better results can be obtained at much lower resolutions with other elements.

Finally, in Fig. 12 we plot the normalised pressure $p^\star = p/(\delta\rho\,g\,L_b)$ at the center of the block (where L_b is the size of the

410 block), as a function of the viscosity ratio $\eta^\star$ in the case where a reduced density field is used. For the $Q_2 \times Q_1$ and the stabilised $Q_1 \times Q_1$ elements, the pressure at this point is uniquely defined since the elements have continuous pressures. For the other two elements the pressure is discontinuous across element edges and it is therefore not uniquely defined at our measurement point. We have then chosen to measure it at four locations corresponding to $(x_c \pm \delta x, y_c \pm \delta y)$ where $\delta x = \delta y = 0.1\mathrm{m}$, and show the normalized pressures at all four of these locations in the figure. For the $Q_2 \times P_{-1}$ element, the difference between

415 these values is negligible, but not so for the $Q_1 \times P_0$ for which the pressure is a stair-step function with very different values depending on which step an evaluation point is on. The distance between the two lines for the $Q_1 \times P_0$ element decreases with mesh refinement (indicating convergence of the pressure to the true value), but only slowly and, matching the observation in Section 5.1, at the cost of not only a fine mesh but also very large numbers of linear solver iterations.

In addition to the slow convergence of the $Q_1 \times P_0$ element, the most striking conclusion of this benchmark is that for

420 buoyancy-driven flows, the solution obtained using the stabilised $Q_1 \times Q_1$ element on typical meshes does not only strongly
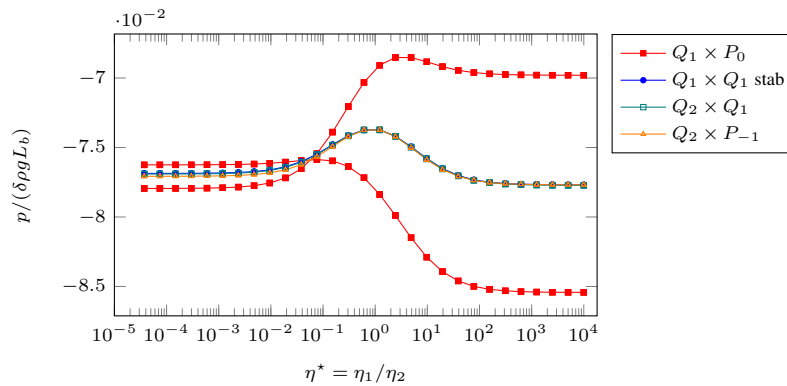
Figure 12. Sinking block benchmark. Normalised pressure $p/(\delta \rho\, g\, L_b)$ in the center of the block as a function of the viscosity ratio $\eta^\star$. These computations use a 256×256 mesh and the reduced density. For the $Q_1 \times P_0$ and $Q_2 \times P_{-1}$ elements with their discontinuous pressure spaces, we show the normalized pressures at several slightly displaced points $(x_c \pm \delta x, y_c \pm \delta y)$. For the $Q_2 \times P_{-1}$ element, the difference is not visible, but for the $Q_1 \times P_0$ this yields the two very different red curves; this is due to the fact that the pressure for this element forms a stair-step function for which two of the evaluation points are on a lower and two on a higher step.

depend on the choice of the otherwise arbitrary reference density, but is also almost entirely unreliable even on meshes that are already quite fine.

6   Numerical results for a model application

While the previous sections have built our intuition for which element may actually work in the context of geodynamics appli-
425 cations, they have only done so through abstract and idealised benchmarks. It is therefore interesting to investigate what one would find in more realistic setups, and consequently we have also investigated convergence for a situation still sufficiently simple that numerical simulations can reach reasonably high accuracy, but that has more of the complexity one would generally find in "real" simulations. Given that the previous examples have highlighted that the stabilised $Q_1 \times Q_1$ element has difficulties with the pressure approximation, we are specifically interested in a situation where the material behaviour is pressure
430 dependent.

To this end, we here consider an example of continental extension. The setup is similar to ones that can be found in Huismans and Beaumont (2002); Jammes and Huismans (2012); Naliboff and Buiter (2015); Brune et al. (2017), and we specifically use the one that can be found in the "continental extension" cookbook of the manual of the ASPECT code (Bangerth et al., 2021). The situation we model here is characterised by the following building blocks: On a domain of size $400\,\mathrm{km} \times 100\,\mathrm{km}$, we impose
435 an extensional horizontal velocity component of $\pm 0.25\,\mathrm{cm/year}$ on the sides, and a vertical upward velocity of $0.125\,\mathrm{cm/year}$ at the bottom. The tangential components are left free. At the top, we allow for a free boundary. More interestingly, we use a pressure- and temperature-dependent visco-plastic rheology of Drucker-Prager type with parameters for viscous deformation

based on dislocation creep flow laws:

$$\eta_{\mathrm{disl}} = A^{-1/n}\dot{\varepsilon}^{-1+1/n}\exp\left(\frac{Q+pV}{nRT}\right) \tag{15}$$

440   where A is a material constant, n is an index typically between 3 and 4, Q is the activation energy, V is the activation volume, R the gas constant, T the temperature and $\dot{\varepsilon}$ is the effective strain rate (the square root of the second invariant of the corresponding tensor). Stresses are limited plastically at a yield stress $\sigma_y = C\cos(\phi) + P\sin(\phi)$ via a Drucker-Prager criterion where C is the cohesion and ϕ the angle of friction. We use distinct values for some of these parameters in the initially $20\,\mathrm{km}$-thick upper crust (wet quartzite), an initially $10\,\mathrm{km}$-thick lower crust (wet anorthite), and the mantle (dry olivine) which initially occupies

445   the remaining $70\,\mathrm{km}$ in depth. Deformation is seeded by a weak area within the mantle lithosphere. We only carry out a single time step as obtained with a CFL number of 0.5.

A complete and concise description of this setup has more parameters than are worth spelling out in detail here. For a detailed description, see Naliboff and Buiter (2015) and the section of the ASPECT manual along with the corresponding input files. For the purposes of this paper, the important part is that both the yield stress and the dislocation creep rheology depend

450   on the pressure; as a consequence, we can anticipate that elements that result in poor pressure accuracy may not yield accurate simulations in general.

This setup produces localised shear zones that accommodate the majority of the deformation. Fig. 13 illustrates the structure of the resulting solution. Each panel of the figure shows in its left half the solution produced by the stabilised $Q_1 \times Q_1$ element and its right half that produced by the Taylor-Hood $Q_2 \times Q_1$ element. Because the solution is symmetric, the two halves should

455   be mirror images. It is, however, clear from several of the panels that this is not the case: the $Q_1 \times Q_1$ element produces large artifacts at depth where the pressure is large and the pressure-dependence of the material strong.

This effect is also demonstrated in a different way in Fig. 14 where we show laterally averaged quantities for the different elements and different mesh resolutions. Even though it is clear from Fig. 13 that lateral averaging should result in a better approximation (than pointwise evaluations) of the correct quantities for a given depth, Fig. 14 shows that even the average

460   is far from correct. On the other hand, the figure shows that with increasing mesh resolution, the solutions produced by the $Q_1 \times Q_1$ seem to converge to the solutions generated by the other elements – albeit very slowly and at what one might consider an unacceptable cost.

To investigate the origin of these convergence problems of the $Q_1 \times Q1$ element, one should recall that the model is nonlinear. As a consequence, the artifacts may be related to the discretisation, or to a failure of the nonlinear iteration – and the two may

465   be connected. All of the solutions we show were taken after 100 Picard iterations to resolve the nonlinearity of the model, with nonlinear convergence shown in Fig. 15. (One could accelerate convergence by using a Newton solver (Fraters et al., 2019), but this is not relevant for the work herein.) Looking at the evolution of the nonlinear residual during these iterations, we see that it decreases quickly and for most element choices then plateaus at about 10^{-5} relative to the starting residual. In contrast, for the stabilised $Q_1 \times Q_1$ element, increasing the mesh resolution yields lower nonlinear residuals – but even on the finest

470   mesh, the nonlinear residuals are still substantially worse than for any of the other elements, with no apparent progress after about 20 iterations.
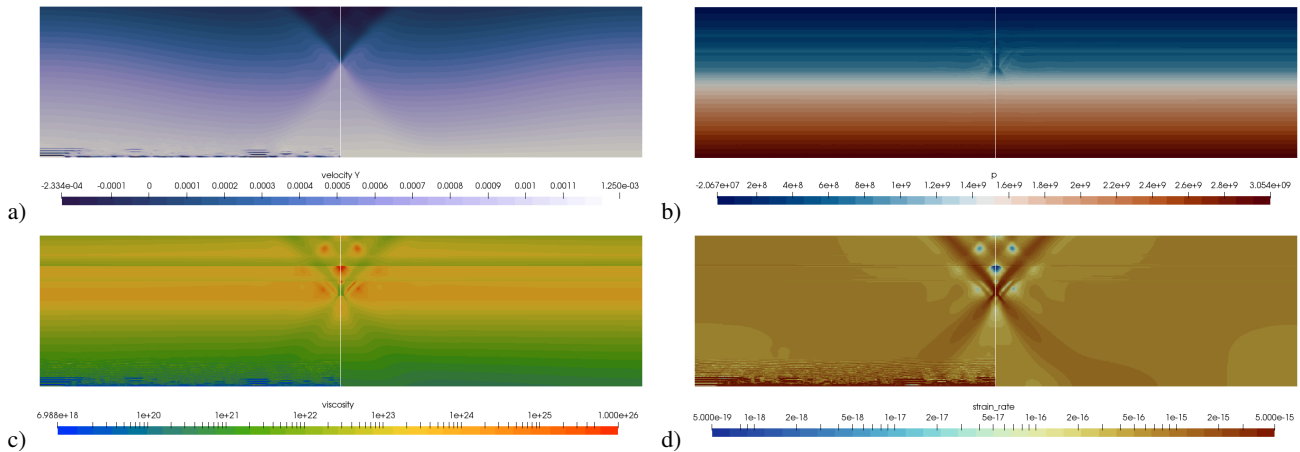
Figure 13. Application example. a) Vertical component of the velocity field; b) pressure field; c) Effective viscosity field; d) Effective Strain rate field. In all figures, the left half (left of the vertical line) shows data obtained with the stabilised $Q_1 \times Q_1$ element, whereas the right half shows results obtained with the $Q_2 \times Q_1$ element. Note the large deviations between the two towards the bottom of the domain. All results were obtained on an 800×200 mesh with a cell size of 0.5 km.
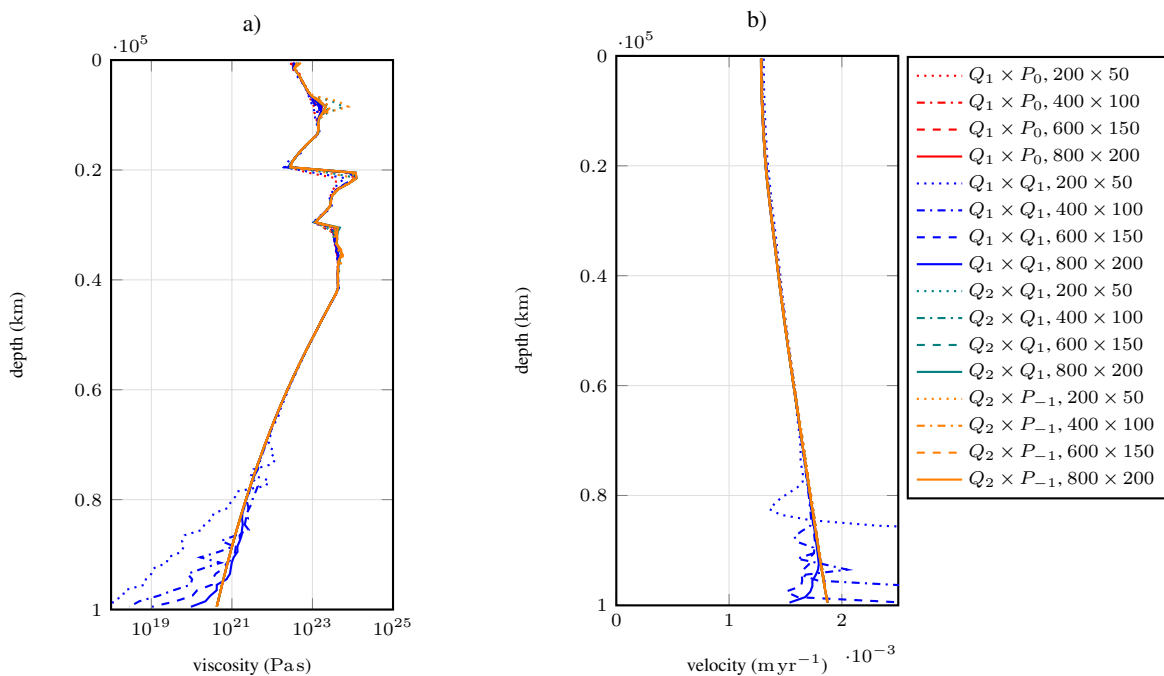

Figure 14. Application example. a) Laterally averaged effective viscosity; b) Laterally averaged velocity magnitude. The line styles chosen become increasingly assertive (dotted to solid lines) as mesh resolution is increased.
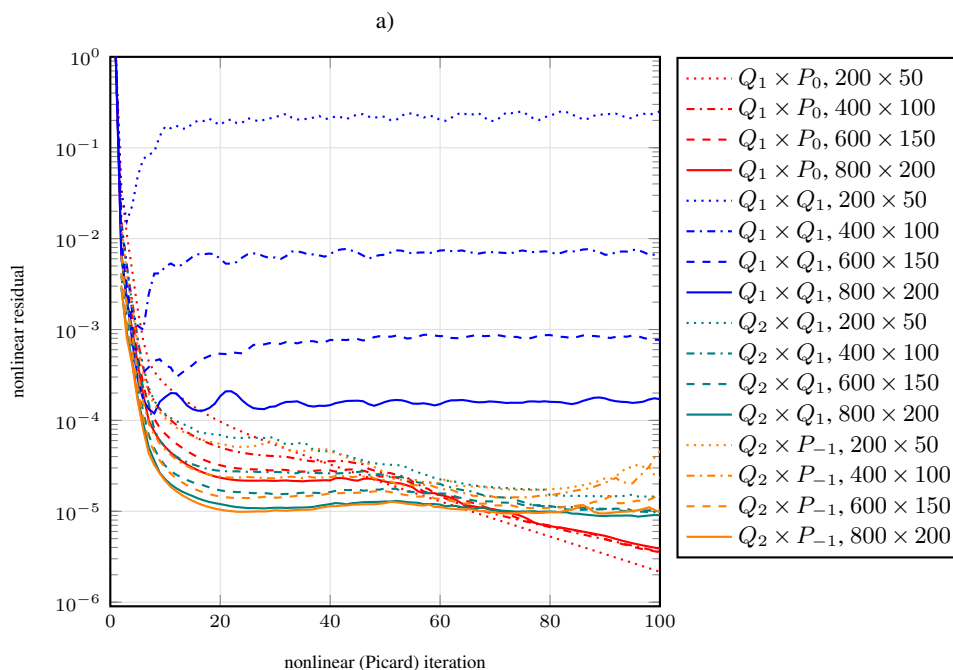
a)

Figure 15. Application example. Nonlinear residual as a function of nonlinear iteration step for all four elements and for different mesh resolutions.

Our interpretation of this experiment is that the inability of the $Q_1 \times Q1$ element to generate accurate pressure fields leads to values for the pressure-dependent rheology that are so far away from their correct values – and, indeed, from the values on nearby cells – that they greatly increase the condition number of the linear systems that have to be solved in each nonlinear iteration. The resulting difficulty of solving these Picard steps accurately then affects the speed with which the nonlinear residual is reduced by the Picard iteration, to the point where the condition number is so large that no convergence can be achieved any more. Only mesh refinement, with the attendant increased accuracy of the pressure solution (and, consequently, a more accurate viscosity) helps in restoring the ability to actually solve this problem to small nonlinear residuals.

7 Conclusions

In this contribution, we have provided a side-by-side comparison of the most widely used quadrilateral finite elements. As outlined in the introduction, most finite element solvers used in the geodynamics community rely on one or the other of these. At the same time, we are not aware of a comprehensive comparison of their relative strengths – or their weaknesses, as they may be.

Using the artificial, linear benchmarks discussed in Section 5, we can infer that when the solution is smooth, the Taylor-Hood variations $Q_2 \times Q_1$ and $Q_2 \times P_{-1}$ provide far better accuracy than the lower-order elements $Q_1 \times P_0$ and the stabilised

$Q_1 \times Q_1$. This advantage is largely lost when one considers problems in which the viscosity is discontinuous. Since we believe that the real Earth has relatively narrow phase transition zones where the viscosity may jump by large factors, benchmarks like the SolVi one in Section 5.3 are relevant and illuminate important aspects.

From these considerations, one may conclude that the Taylor-Hood variations are too expensive – in terms of their number

490   of degrees of freedom and the attendant memory and CPU time cost. However, we believe that this is not so:

-   For buoyancy-driven flows such as the sinking block benchmark in Section 5.4, the stabilised $Q_1 \times Q_1$ element is largely unable to reproduce the correct solution and, furthermore, depends on using a formulation in which one subtracts a reference density from the actual density; this is equivalent to defining a hydrostatic pressure profile and only attempting to solve for the "dynamic" component of the pressure. Crucially, however, there are many ways of defining such a

495   reference density, neither of which is canonical and "obviously right" in complex mantle convection simulations. Since the solution obtained with the stabilised $Q_1 \times Q_1$ element strongly depends on the specific choice of reference density, we conclude that the element cannot be made robust for the kinds of flows we encounter in real mantle convection situations. We have also verified this assertion using an application where we consider continental extension (Section 6), and where the inability to produce accurate pressure solutions also greatly affects the convergence of the nonlinear solver, to the

500   point where the computed solution must be considered unusable. We have shown that these errors can be reduced when choosing *very* fine meshes, but the attendant cost is unacceptable when compared with that of using other elements on far coarser meshes.

    There are other considerations to believe that the procedure of trying to subtract a reference density (or a hydrostatic pressure) can not be a successful strategy. For example, simulations of free or deformable surfaces (at the Earth surface

505   as well as at the core-mantle boundary) require accurate knowledge of the total pressure. This is true for coupled formulations of flow and surface deformation (Rose et al., 2017) and approaches such as the "sticky air" method (Crameri et al., 2012). But similar considerations also apply to nonlinear material laws in which the pressure enters the viscosity or, more commonly, phase computations that determine the density and other thermodynamic material properties from the pressure and the temperature. Indeed, one could conjecture that the stabilised $Q_1 \times Q_1$ element would also fail for

510   compressible Stokes simulations, though we have not verified this here.

    We conclude from these thoughts that the stabilised $Q_1 \times Q_1$ element is not a viable choice for mantle convection simulations. It is important to point out that the cases we consider as crucial here – buoyancy-driven flows, large hydrostatic pressures, and pressure-dependent rheologies – are uncommon on most of the engineering applications for which the $Q_1 \times Q_1$ was originally developed; as a consequence, it is not surprising that what we find here contradicts substantial

515   parts of the engineering literature where the element remains widely used.

-   We believe that the $Q_1 \times P_0$ element is also not a viable choice. As shown by several of the analytical benchmarks, the errors that result from using this element can be orders of magnitude larger than the corresponding errors that result from the Taylor-Hood-type elements. This is no longer the case once we consider discontinuous viscosity profiles (see Section 5.3), but this element is also unable to accurately solve the buoyancy-driven case discussed in Section 5.4.

520   Furthermore, as pointed out before, this element is not LBB-stable which, despite considerable efforts in the past decades, has limited its use in combination with iterative methods: because of the corresponding condition number increase, the number of iterations is found to grow in a somewhat unpredictable manner with an increase in resolution. This may explain why, despite the Citcom codes' success over two decades with studies based on models counting up to ∼100M elements on several hundreds of processors (e.g. Jadamec and Billen, 2012), the current generation of massively parallel

525   codes relies on either stable (Kronbichler et al., 2012; May et al., 2015) or stabilised elements (Burstedde et al., 2013), or uses the finite difference method (Kaus et al., 2016).

In summary, we think that the Taylor-Hood variations $Q_2 \times Q_1$ and $Q_2 \times P_{-1}$ present the best compromise for robust mantle convection and crustal dynamics simulations. This is not because these elements are "obviously better" than the others, but due more to a "last man standing" argument: The other choices simply disqualified themselves by failing to provide adequate

530   accuracy in one situation or another. At the same time, the lack of regularity one expects of typical scenarios also implies that we should not expect higher-order Taylor-Hood elements $Q_{k+1} \times Q_k$ or $Q_{k+1} \times P_{-k}$ with $k > 2$ to provide substantially better accuracy compared to their much higher computational cost. Although we have only shown results for two-dimensional simulations, experience – including the experience with the ASPECT code used here that solves two- and three-dimensional problems within the same framework – suggests that all of these considerations would also apply to the three-dimensional

535   (hexahedral) analogs of the ones we have used.

Of course, the choices we have considered here are not the only ones. One could, for example, consider "simplicial" (triangular and tetrahedral) elements instead of the quadrilateral and hexahedral ones we have used here. Indeed, some existing mantle convection codes use this strategy. One successful example is the TERRA-NEO code that uses equal-order linear tetrahedra (Gmeiner et al., 2015; Weismüller et al., 2015) stabilised by means of a pressure-stabilisation approach based on the addition of

540   linear least-squares terms (the "PSPG" approach, see Brezzi and Douglas (1988); Elman et al. (2014)); other examples include Fluidity (Davies et al., 2011) and LaCoDe (de Montserrat et al., 2019). While we have not evaluated simplicial elements, one might conjecture that many of the same conclusions would also hold: The unstable $P_1 \times P_0$ provides low accuracy and is unstable, the stabilised $P_1 \times P_1$ has difficulties with buoyancy-driven flows and large hydrostatic pressures, and the Taylor-Hood element $P_2 \times P_1$ is expensive but robust.

545   Finally, there are other, more exotic elements one could work with. Examples include the Rannacher-Turek element (Rannacher and Turek, 1992), the Crouzeix-Raviart element (Crouzeix and Raviart, 1973), or the DSSY element (Douglas et al., 1999). We have not investigated these kinds of choices for four reasons: (i) The manuscript at hand is long enough as it stands, (ii) these elements are not widely used, both within and outside our community, and (iii) many of these elements are difficult to implement in one regard or another, including complications with boundary conditions and with dealing with unstructured and

550   possibly curvilinear cells; finally, (iv) the elements mentioned above are not as widely available or completely implemented in common software frameworks, and their use thus requires substantial additional implementation work.

While we have not investigated these two possible directions for alternatives to the elements we have considered, we think that such studies would be interesting. We hope that our careful choice of test cases might also be useful to such studies.

Author contributions. CT conceived the study and ran all models. WB implemented the stabilised $Q_1 \times Q_1$ element in ASPECT. Both authors discussed the results and and jointly wrote the manuscript.

Competing interests. The authors declare that they have no conflict of interest.

References

565 Alisic, L., Gurnis, M., Stadler, G., Burstedde, C., and Ghattas, O.: Multi-scale dynamics and rheology of mantle flow with plates, J. Geo-
       phys. Res., 117, https://doi.org/10.1029/2012JB009234, 2012.

Arndt, D., Bangerth, W., Davydov, D., Heister, T., Heltai, L., Kronbichler, M., Maier, M., Pelteret, J.-P., Turcksin, B., and
       Wells, D.: The deal. II finite element library: Design, features, and insights, Computers & Mathematics with Applications,
       https://doi.org/10.1016/j.camwa.2020.02.022, 2020.

570 Arrial, P.-A. and Billen, M.: Influence of geometry and eclogitization on oceanic plateau subduction , Earth Planet. Sci. Lett., 363, 34–43,
       https://doi.org/10.1016/j.epsl.2012.12.011, 2013.

Bangerth, W., Hartmann, R., and Kanschat, G.: deal.II - a general purpose object oriented finite element library, ACM Transaction on
       mathematical software, 33, https://doi.org/10.1145/1268776.1268779, 2007.

Bangerth, W., Heister, T., et al.: ASPECT: Advanced Solver for Problems in Earth's ConvecTion, Computational Infrastructure for Geody-
575   namics, 2021.

Bochev, P. B., Dohrmann, C. R., and Gunzburger, M. D.: Stabilization of Low-order Mixed Finite Elements for the Stokes Equations, SIAM
       Journal on Numerical Analysis, 44, 82–101, https://doi.org/10.1137/s0036142905444482, 2006.

Braun, J., Thieulot, C., Fullsack, P., DeKool, M., and Huismans, R.: DOUAR: a new three-dimensional creeping flow model for the solution
       of geological problems, Phys. Earth. Planet. Inter., 171, 76–91, 2008.

580 Brezzi, F. and Douglas, J.: Stabilised mixed methods for the Stokes problem, Numer. Math., 53, 225–235, 1988.

Brezzi, F. and Pitkäranta, J.: On the stabilization of finite element approximations of the Stokes equations, vol. 10 of *Notes on numerical
       fluid mechanics*, pp. 11–19, Vieweg+Teubner Verlag, https://doi.org/10.1007/978-3-663-14169-3_2, 1984.

Brune, S., Heine, C., Clift, P. D., and Pérez-Gussinyé, M.: Rifted margin architecture and crustal rheology: reviewing Iberia-Newfoundland,
       central South Atlantic, and South China sea, Marine and Petroleum Geology, 79, 257–281, 2017.

585 Burstedde, C., Ghattas, O., Stadler, G., Tu, T., and Wilcox, L.: Parallel scalable adjoint-based adaptive solution of variable-viscosity Stokes
       flow problems, Computer Methods in Applied Mechanics and Engineering, 198, 1691–1700, https://doi.org/10.1016/j.cma.2008.12.015,
       2009.

Burstedde, C., Stadler, G., Alisic, L., Wilcox, L., Tan, E., Gurnis, M., and Ghattas, O.: Large-scale adaptive mantle convection simulation,
       Geophy. J. Int., 192, 889–906, https://doi.org/10.1093/gji/ggs070, 2013.

590 Cerpa, N., Hassani, R., Gerbault, M., and Prévost, J.-H.: A fictitious domain method for lithosphere-asthenosphere interaction: Application
       to periodic slab folding in the upper mantle, Geochem. Geophys. Geosyst., 15, 2014.

Cerpa, N., Araya, R., Gerbault, M., and Hassani, R.: Relationship between slab dip and topography segmentation in an oblique subduction
       zone: Insights from numerical modeling, Geophys. Res. Lett., 41, 10.1002/2015GL064 047, 2015.

Cerpa, N., Guillaume, B., and J.Martinod: The interplay between overriding plate kinematics, slab dip and tectonics, Geophy. J. Int., 215,
595   1789–1802, 2018.

Clevenger, T., Heister, T., Kanschat, G., and Kronbichler, M.: A flexible, parallel, adaptive geometric multigrid method for FEM, ACM
       Trans. Math. Softw. 47, https://doi.org/10.1145/3425193, 2020.

Crameri, F., Schmeling, H., Golabek, G., Duretz, T., Orendt, R., Buiter, S., May, D., Kaus, B., Gerya, T., and Tackley, P.: A comparison of
       numerical surface topography calculations in geodynamic modelling: an evaluation of the 'sticky air' method, Geophy. J. Int., 189, 38–54,
600   2012.

Crouzeix, M. and Raviart, P.-A.: Conforming and nonconforming finite element methods for solving the stationary Stokes equations I, R.A.I.R.O., 7, 33–75, 1973.

Davies, D., Wilson, C., and Kramer, S.: Fluidity: A fully unstructured anisotropic adaptive mesh computational modeling framework for geodynamics, Geochem. Geophys. Geosyst., 12, https://doi.org/10.1029/2011GC003551, 2011.

605 de Montserrat, A., Morgan, J. P., and Hasenclever, J.: LaCoDe: a Lagrangian two-dimensional thermo-mechanical code for large-strain compressible visco-elastic geodynamical modeling, Tectonophysics, p. 228173, 2019.

Deubelbeiss, Y. and Kaus, B.: Comparison of Eulerian and Lagrangian numerical techniques for the Stokes equations in the presence of strongly varying viscosity, Phys. Earth Planet. Interiors, 171, 92–111, https://doi.org/10.1016/j.pepi.2008.06.023, 2008.

Dohrmann, C. and Bochev, P.: A stabilized finite element method for the Stokes problem based on polynomial pressure projections,
610 Int. J. Num. Meth. Fluids, 46, 183–201, https://doi.org/10.1002/d.752, 2004.

Donea, J. and Huerta, A.: Finite Element Methods for Flow Problems, John Wiley & Sons, 2003.

Douglas, J., Santos, J. E., Sheen, D., and Ye, X.: Nonconforming Galerkin methods based on quadrilateral elements for second order elliptic problems, ESAIM: Mathematical Modelling and Numerical Analysis, 33, 747–770, 1999.

Duretz, T., May, D., Gerya, T., and Tackley, P.: Discretization errors and free surface stabilisation in the finite difference and marker-in-cell
615 method for applied geodynamics: A numerical study, Geochem. Geophys. Geosyst., 12, https://doi.org/10.1029/2011GC003567, 2011.

Elman, H., Silvester, D., and Wathen, A.: Finite Elements and Fast Iterative Solvers, Oxford Science Publications, 2014.

Fraters, M., Bangerth, W., Thieulot, C., Glerum, A., and Spakman, W.: Efficient and Practical Newton Solvers for Nonlinear Stokes Systems in Geodynamic Problems, Geophy. J. Int., https://doi.org/10.1093/gji/ggz183, 2019.

Fullsack, P.: An arbitrary Lagrangian-Eulerian formulation for creeping flows and its application in tectonic models, Geophy. J. Int., 120,
620 1–23, https://doi.org/10.1111/j.1365-246X.1995.tb05908.x, 1995.

Gerya, T.: Numerical Geodynamic Modelling, Cambridge University Press, 2010.

Gerya, T., May, D., and Duretz, T.: An adaptive staggered grid finite difference method for modeling geodynamic Stokes flows with strongly variable viscosity, Geochem. Geophys. Geosyst., 14, https://doi.org/10.1002/ggge.20078, 2013.

Gmeiner, B., Rüde, U., Stengel, H., Waluga, C., and Wohlmuth, B.: Performance and scalability of hierarchical hybrid multigrid solvers for
625 Stokes systems, SIAM Journal on Scientific Computing, 37, C143–C168, https://doi.org/10.1137/130941353, 2015.

Gresho, P. and Sani, R.: Incompressible flow and the Finite Element Method, vol II, John Wiley and Sons, Ltd, 2000.

Gresho, P., Chan, S., Christon, M., and Hindmarsch, A.: A little more on stabilised Q_1Q_1 for transient viscous incompressible flow, Int. J. Num. Meth. Fluids, 21, 837–856, 1995.

Heister, T., Dannberg, J., Gassmöller, R., and Bangerth, W.: High Accuracy Mantle Convection Simulation through Modern Numerical
630 Methods. II: Realistic Models and Problems, Geophy. J. Int., 210, 833–851, https://doi.org/10.1093/gji/ggx195, 2017.

Huismans, R. and Beaumont, C.: Complex rifted continental margins explained by dynamical models of depth-dependent lithospheric extension, Geology, 30, 211–214, 2002.

Jadamec, M. and Billen, M.: The role of rheology and slab shape on rapid mantle flow: Three-dimensional numerical models of the Alaska slab edge, J. Geophys. Res., 117, 2012.

635 Jammes, S. and Huismans, R.: Structural styles of mountain building: Controls of lithospheric rheologic stratification and extensional inheritance, J. Geophys. Res., 117, 2012.

Kaus, B., Mühlhaus, H., and May, D.: A stabilization algorithm for geodynamic numerical simulations with a free surface, Phys. Earth. Planet. Inter., 181, 12–20, https://doi.org/10.1016/j.pepi.2010.04.007, 2010.

Kaus, B., Popov, A., Baumann, T., Pusok, A., Bauville, A., Fernandez, N., and Collignon, M.: Forward and Inverse Modelling of Lithospheric
640   Deformation on Geological Timescales, NIC Symposium 2016, pp. 299–307, 2016.

King, S., Raefsky, A., and Hager, B.: ConMan: Vectorizing a finite element code for incompressible two-dimensional convection in the
       Earth's mantle, Phys. Earth. Planet. Inter., 59, 195–208, https://doi.org/10.1016/0031-9201(90)90225-M, 1990.

Kronbichler, M., Heister, T., and Bangerth, W.: High accuracy mantle convection simulation through modern numerical methods , Geo-
       phy. J. Int., 191, 12–29, https://doi.org/10.1111/j.1365-246X.2012.05609.x, 2012.

645   Le Pourhiet, L., Huet, B., May, D., Labrousse, L., and Jolivet, L.: Kinematic interpretation of the 3D shapes of metamorphic core complexes,
       Geochem. Geophys. Geosyst., 13, https://doi.org/10.1029/2012GC004271, 2012.

Lehmann, R., Lukacova-Medvidova, M., Kaus, B., and Popov, A.: Comparison of continuous and discontinuous Galerkin approaches for
       variable-viscosity Stokes flow, Z. Angew. Math. Mech., pp. 1–14, https://doi.org/10.1002/zamm.201400274, 2015.

Leng, W. and Zhong, S.: Implementation and application of adaptive mesh refinement for thermochemical mantle convection studies,
650   Geochem. Geophys. Geosyst., 12, https://doi.org/10.1029/2010GC003425, 2011.

May, D. and Moresi, L.: Preconditioned iterative methods for Stokes flow problems arising in computational geodynamics,
       Phys. Earth. Planet. Inter., 171, 33–47, https://doi.org/10.1016/j.pepi.2008.07.036, 2008.

May, D., Brown, J., and Le Pourhiet, L.: A scalable, matrix-free multigrid preconditioner for finite element discretizations of heterogeneous
       Stokes flow, Computer Methods in Applied Mechanics and Engineering, 290, 496–523, https://doi.org/10.1016/j.cma.2015.03.014, 2015.

655   McNamara, A. K. and Zhong, S.: Thermochemical structures within a spherical mantle: Superplumes or piles?, Journal of Geophysical
       Research: Solid Earth, 109, https://doi.org/10.1029/2003JB002847, 2004.

Mishin, Y.: Adaptive multiresolution methods for problems of computational geodynamics, Ph.D. thesis, ETH Zurich, 2011.

Moresi, L. and Gurnis, M.: Constraints on the lateral strength of slabs from three-dimensional dynamic flow models, Earth and Planetary
       Science Letters, 138, 15–28, https://doi.org/10.1016/0012-821X(95)00221-W, 1996.

660   Moresi, L., Dufour, F., and Mühlhaus, H.: A Lagrangian integration point finite element method for large deformation modeling of visco-
       elastic geomaterials, J. Comp. Phys., 184, 476–497, https://doi.org/10.1016/S0021-9991(02)00031-1, 2003.

Moresi, L., Landry, W., Hodkison, L., Turnbull, R., Lemiale, V., May, D., Stegman, D., Velic, M., Sunter, P., and Giordani, J.: Gale v2.0.1,
       2012.

Naliboff, J. and Buiter, S.: Rift reactivation and migration during multiphase extension, Earth Planet. Sci. Lett., 421, 58–67, 2015.

665   Norburn, S. and Silvester, D.: Fourier analysis of stabilized Q1-Q1 mixed finite element approximation, SIAM J. Numer. Anal., 39, 817–833,
       https://doi.org/10.1137/S0036142999362274, 2001.

O'Neill, C., Moresi, L., Müller, D., Albert, R., and Dufour, F.: Ellipsis 3D: a particle-in-cell finite element hybrid code for modelling mantle
       convection and lithospheric deformation, Computers and Geosciences, 32, 1769–1779, 2006.

Plunder, A., Thieulot, C., and van Hinsbergen, D.: The effect of obliquity on temperature in subduction zones: insights from 3D numerical
670   modeling, Solid Earth, 9, 759–776, https://doi.org/10.5194/se-2017-134, 2018.

Popov, A. and Sobolev, S.: SLIM3D: a tool for three-dimensional thermomechanical modelling of lithospheric deformation with elasto-
       visco-plastic rheology, Phys. Earth. Planet. Inter., 171, 55–75, https://doi.org/10.1016/j.pepi.2008.03.007, 2008.

Rannacher, R. and Turek, S.: Simple Nonconforming Quadrilateral Stokes Element, Numerical Methods for Partial Differential Equations,
       8, 97–111, 1992.

675   Rose, I., Buffet, B., and Heister, T.: Stability and accuracy of free surface time integration in viscous flows, Phys. Earth. Planet. Inter., 262,
       90–100, 2017.

Sani, R., Gresho, P., Lee, R., and Griffiths, D.: The cause and cure (?) of the spurious pressures generated by certain FEM solutions of the incompressible Navier-Stokes equations: part 1, Int. J. Num. Meth. Fluids, 1, 17–43, https://doi.org/10.1002/fld.1650010104, 1981a.

Sani, R., Gresho, P., Lee, R., Griffiths, D., and Engelman, M.: The cause and cure (?) of the spurious pressures generated by certain FEM solu-
680   tions of the incompressible Navier-Stokes equations: part 2, Int. J. Num. Meth. Fluids, 1, 171–204, https://doi.org/10.1002/fld.1650010206, 1981b.

Schmid, D. and Podlachikov, Y.: Analytical solutions for deformable elliptical inclusions in general shear, Geophy. J. Int., 155, 269–288, https://doi.org/10.1046/j.1365-246X.2003.02042.x, 2003.

Schubert, G., Turcotte, D., and Olson, P.: Mantle Convection in the Earth and Planets, Cambridge University Press, 2001.

685 Schuh-Senlis, M., Thieulot, C., Cupillard, P., and Caumon, G.: Towards the application of Stokes flow equations to structural restoration simulations, Solid Earth, 11, 1909–1930, https://doi.org/10.5194/se-11-1909-2020, 2020.

Silvester, D. and Kechkar, N.: Stabilised bilinear-constant velocity-pressure finite elements for the conjugate gradient solution of the stokes problem, Computer Methods in Applied Mechanics and Engineering, 79, 71–86, https://doi.org/10.1016/0045-7825(90)90095-4, 1990.

Stadler, G., Gurnis, M., Burstedde, C., Wilcox, L., Alisic, L., and Ghattas, O.: The dynamics of plate tectonics and mantle flow: from local
690   to global scales, Science, 329, 1033–1038, https://doi.org/10.1126/science.1191223, 2010.

Suckale, J., Nave, J.-C., and Hager, B.: It takes three to tango: 1. Simulating buoyancy-driven flow in the presence of large viscosity contrasts, J. Geophys. Res., 115, https://doi.org/10.1029/2009JB006916, 2010.

Thielmann, M., May, D., and Kaus, B.: Discretization errors in the Hybrid Finite Element Particle-In-Cell Method, Pure and Applied Geo-
physics, 171, 2164–2184, https://doi.org/10.1007/s00024-014-0808-9, 2014.

695 Thieulot, C.: FANTOM: two- and three-dimensional numerical modelling of creeping flows for the solution of geological problems, Phys. Earth. Planet. Inter., 188, 47–68, https://doi.org/10.1016/j.pepi.2011.06.011, 2011.

Thieulot, C.: ELEFANT: a user-friendly multipurpose geodynamics code, Solid Earth Discussions, 6, 1949–2096, 2014.

Thieulot, C., Fullsack, P., and Braun, J.: Adaptive octree-based finite element analysis of two- and three-dimensional indentation problems, J. Geophys. Res., 113, B12 207, https://doi.org/10.1029/2008JB005591, 2008.

700 Turcotte, D. and Schubert, G.: Geodynamics, 2nd edition, Cambridge, 2012.

Turek, S.: Efficient Solvers for Incompressible Flow Problems, Springer, 1999.

Weismüller, J., Gmeiner, B., Ghelichkhan, S., Huber, M., John, L., Wohlmuth, B., Rüde, U., and Bunge, H.-P.: Fast asthenosphere motion in high-resolution global mantle flow models, Geophysical Research Letters, 42, 7429–7435, https://doi.org/10.1002/2015GL063727, 2015.

Zhong, S.: Analytic solutions for Stokes' flow with lateral variations in viscosity, Geophys. J. Int., 124, 18–28, https://doi.org/10.1111/j.1365-
705   246X.1996.tb06349.x, 1996.

Zhong, S.: Constraints on thermochemical convection of the mantle from plume heat flux, plume excess temperature, and upper mantle temperature, Journal of Geophysical Research, 111, https://doi.org/10.1029/2005JB003972, 2006.

Zhong, S., Zuber, M., Moresi, L., and Gurnis, M.: The role of temperature-dependent viscosity and surface plates in spherical shell models of mantle convection, J. Geophys. Res., 105, 11,063–11,082, https://doi.org/10.1029/2000JB900003, 2000.

710 Zhong, S., McNamara, A., Tan, E., Moresi, L., and Gurnis, M.: A benchmark study on mantle convection in a 3-D spherical shell using CitcomS, Geochem. Geophys. Geosyst., 9, https://doi.org/10.1029/2008GC002048, 2008.

Zienkiewicz, O. and Taylor, R.: The Finite Element Method. Vol. 1: The basis, Butterworth and Heinemann, 2002.